Transfer learning in a biomaterial fibrosis model identifies in vivo senescence heterogeneity and contributions to vascularization and matrix production across species and diverse pathologies

Cherry, Christopher; Andorko, James I.; Krishnan, Kavita; Mejías, Joscelyn C.; Nguyen, Helen Hieu; Stivers, Katlin B.; Gray-Gaillard, Elise F.; Ruta, Anna; Han, Jin; Hamada, Naomi

Published in:
GeroScience

DOI:
10.1007/s11357-023-00785-7

Publication date:
2023

GeroScience (2023) 45:2559–2587
https://doi.org/10.1007/s11357-023-00785-7

ORIGINAL ARTICLE

Transfer learning in a biomaterial fibrosis model identifies in vivo senescence heterogeneity and contributions to vascularization and matrix production across species and diverse pathologies

Christopher Cherry · James I. Andorko · Kavita Krishnan · Joscelyn C. Mejías · Helen Hieu Nguyen · Katlin B. Stivers · Elise F. Gray-Gaillard · Anna Ruta · Jin Han · Naomi Hamada · Masakazu Hamada · Ines Sturmlechner · Shawn Trewartha · John H. Michel · Locke Davenport Huyer · Matthew T. Wolf · Ada J. Tam · Alexis N. Peña · Shilpa Keerthivasan · Claude Jordan Le Saux · Elana J. Fertig · Darren J. Baker · Franck Housseau · Jan M. van Deursen · Drew M. Pardoll · Jennifer H. Elisseeff

Received: 1 February 2023 / Accepted: 26 March 2023 / Published online: 20 April 2023

Abstract Cellular senescence is a state of permanent growth arrest that plays an important role in wound healing, tissue fibrosis, and tumor suppression. Despite senescent cells' (SnCs) pathological role and therapeutic interest, their phenotype in vivo remains poorly defined. Here, we developed an in vivo–derived senescence signature (SenSig) using a foreign body response–driven fibrosis model in a *p16-CreER^{T2};Ai14* reporter mouse. We identified pericytes and "cartilage-like" fibroblasts as senescent and defined cell type–specific senescence-associated secretory phenotypes (SASPs). Transfer learning and senescence scoring identified these two SnC populations along with endothelial and epithelial SnCs in new and publicly available murine and human data single-cell RNA sequencing (scRNAseq) datasets from diverse pathologies. Signaling analysis uncovered crosstalk between SnCs and myeloid cells via an IL34–CSF1R–TGFβR signaling axis, contributing to tissue balance of vascularization and matrix production. Overall, our study provides a senescence

Supplementary Information The online version contains supplementary material available at https://doi.org/10.1007/s11357-023-00785-7.

C. Cherry · J. I. Andorko · K. Krishnan · J. C. Mejías · H. H. Nguyen · K. B. Stivers · E. F. Gray-Gaillard · A. Ruta · J. Han · J. H. Michel · L. Davenport Huyer · A. N. Peña · J. H. Elisseeff
Translational Tissue Engineering Center, Wilmer Eye Institute and the Department of Biomedical Engineering, Johns Hopkins University School of Medicine, Baltimore, MD, USA

N. Hamada · M. Hamada · I. Sturmlechner · S. Trewartha · D. J. Baker · J. M. van Deursen
Department of Pediatric and Adolescent Medicine, Mayo Clinic, Rochester, MN, USA

I. Sturmlechner
Department of Pediatrics, Molecular Genetics Section, University of Groningen, University Medical Center Groningen, Antonius Deusinglaan 1, 9713 AV Groningen, Netherlands

M. T. Wolf
Laboratory of Cancer Immunometabolism, Center for Cancer Research, National Cancer Institute, Frederick, MD, USA

A. J. Tam
Department of Oncology, Johns Hopkins University School of Medicine, Baltimore, MD, USA

A. J. Tam · F. Housseau · D. M. Pardoll · J. H. Elisseeff (✉)
Bloomberg~Kimmel Institute for Cancer Immunotherapy and Sidney Kimmel Comprehensive Cancer Center, Johns Hopkins University School of Medicine, Baltimore, MD, USA
e-mail: jhe@jhu.edu

signature and a computational approach that may be broadly applied to identify SnC transcriptional profiles and SASP factors in wound healing, aging, and other pathologies.

Keywords Senescence · RNA sequencing · Fibrosis

Senescent cells (SnCs) are actively implicated in multiple age-related pathologies including heart disease, diabetes, neurodegeneration, cancer, and fibrosis [1–7]. Despite the central role of SnCs in these conditions, and as potential targets for therapeutic intervention, the phenotype and function of SnCs in vivo remains elusive due to challenges with the identification and isolation of these cells. Moreover, the physiological function of SnCs during embryological development and wound healing suggests heterogeneity in phenotype and function, further underscoring the importance of understanding the diverse context-dependent senescence phenotypes that define beneficial versus pathologic senescence [2, 8, 9]. Developing an in-depth understanding of SnCs in health and disease will enable efficient therapeutic targeting of these cells and their secretome, commonly termed the senescence-associated secretory phenotype (SASP).

SnCs are identified by markers, particularly expression of the cell cycle gate keeper $p16^{Ink4a}$, and secretion of the SASP. SnCs influence their microenvironment through the SASP which includes many immunologically relevant molecules such as interleukin (IL)-6, IL1-β, and CCL2 [10–12]. To date, phenotypical characterization of SnCs primarily relied on in vitro methods to induce senescence such as high-dose gamma irradiation, oncogene induction, drug-induced oxidative damage, and proliferative senescence [13–15]. While SnCs and their impact on tissue physiology can be identified in vivo by immunofluorescence and using transgenic animals, there are no widely applicable markers to effectively and comprehensively identify these cells to further characterize their phenotype and secretome [16–18]. Research efforts are now focused on the development of a senescence signature or groups of signatures to accomplish this goal.

Single-cell RNA sequencing and other single-cell "omics" technologies have enabled our understanding of cellular heterogeneity in tissue and tumor microenvironments that are not accessible by bulk methodologies [19–21]. This technology also facilitates discovery of diverse and cell type–specific intercellular interactions, a feature which is appealing for the study of a cell population which is canonically active largely through secretion of signaling proteins [22, 23]. However, identification of SnC in scRNAseq data sets is challenging due to its inherently low depth of scRNAseq that leads to dropout, whereby genes with lower abundance cannot be reliably identified [24]. This limits our ability to identify SnCs in scRNAseq data sets using the common marker gene *Cdkn2a*, the gene that encodes $p16^{Ink4a}$, due to its low levels of expression in a small number of cells. Transfer learning analyses, which can leverage small expression changes across hundreds of genes, may provide an opportunity to identify SnC in scRNAseq data sets despite dropout and have been shown to robustly identify preserved biological processes across tissues, diseases, and species assessed

S. Keerthivasan
Tumor Microenvironment Thematic Research Center, Bristol Myers Squibb, San Francisco, CA, USA

C. J. Le Saux
Department of Medicine, University of California, San Francisco, San Francisco, CA, USA

E. J. Fertig
Department of Biomedical Engineering and Institute for Cell Engineering, Johns Hopkins University School of Medicine, Baltimore, MD, USA

E. J. Fertig
Department of Applied Mathematics and Statistics, Johns Hopkins University, Baltimore, MD, USA

E. J. Fertig
Convergence Institute, Johns Hopkins University School of Medicine, Baltimore, MD, USA

D. J. Baker · J. M. van Deursen
Department of Biochemistry and Molecular Biology, Mayo Clinic, Rochester, MN, USA

D. J. Baker
Paul F. Glenn Center for the Biology of Aging Research at Mayo Clinic, Rochester, MN, USA

by different techniques [25, 26]. This strategy provides the potential to identify SnCs based upon gene signatures in place of isolated gene or protein markers to query their phenotype and function in atlas data sets from diverse biomedical contexts. With a robust senescence signature and transfer learning, cells that have an expression profile similar to p16-expressing cells but do not express *Cdkn2a* can be identified.

Here, we present a new approach for identifying physiologically relevant SnCs in vivo across tissues, conditions, and species. Biomaterials induce fibrosis through the foreign body response (FBR), recapitulating elements of fibrosis observed in SnC-driven pathologies and tissue aging [27]. We previously demonstrated that SnCs and chronic inflammation, including a type 3 immune response, are present in FBR-induced fibrosis [22]. Combining the FBR fibrosis model with a novel $p16^{ink4a}$-marked tdTomato (tdTom) reporter mouse, we were able to identify and characterize SnCs in vivo. The phenotype of $p16^{ink4a}$-expressing cells was identified and sorted for sequencing to develop a comprehensive SnC gene expression signature. Remarkably, when we then used a transfer learning technique to score mouse and human scRNAseq data sets for concordance with the expression signature, we identified two specific stromal cell types as the major cell types that constitute the SnCs. The resulting senescent signature, or SenSig, can indicate populations of cells with SnC expression patterns. It is also possible to determine genes responsible for the elevated score within a given population. Application of the SenSig transfer learning method to new murine and human synthetic implant scRNAseq data sets defined two clusters of senescent stromal cells: pericytes and a cartilage-like fibroblast involved in fibrosis. We further applied the SenSig method to publicly available data sets including human-derived data sets of idiopathic pulmonary fibrosis (IPF) and basal cell carcinoma, confirming broad applicability and elements of a conserved signature. Subsequently, via intercellular signaling analysis and in vitro co-culture assays, we found and validated specific signaling patterns between SnCs and myeloid cells during wound healing and fibrosis through a TGFβ-reliant signaling axis. Overall, the SenSig identifies a conserved transcriptional profile of SnCs that may be broadly applied to identify and understand senescence across a range of diseases. The ability to identify SnCs in the multitude of publicly available single-cell and bulk data sets will enable understanding of senescence phenotype, conserved and tissue-specific SASPs, and subsequent interactions with other cell types contributing to tissue homeostasis and pathology.

Results

Generation of an in vivo *senescence signature from the foreign body response using a* $p16^{ink4a}$ *marked tdTomato (tdTom) reporter mouse*

Previously, we demonstrated the development of SnCs during the FBR to a biomaterial implant in both murine models and clinical samples [22]. To further characterize SnCs in vivo, we implanted polymeric particles composed of poly(caprolactone) (PCL) to induce fibrosis in a muscle wound and enrich the number of SnCs (Fig. 1A). We then measured mRNA levels of *Cdkn2a*, which encodes the $p16^{ink4a}$ protein, a classical marker for senescence. qPCR analysis showed that *Cdkn2a* mRNA increased significantly in the muscle tissue 1 week after injury with or without an implant, confirming wound-induced senescence (Fig. 1B, left). After 6 weeks, when fibrosis around the implant matures, *Cdkn2a* expression significantly increased in the whole tissue containing the PCL implant compared to the wound alone (Fig. 1B, left). FACS-isolated $CD45^{-}CD31^{-}CD29^{+}$ stromal cells from both saline- and PCL-treated injured muscle tissue had a greater than tenfold increase in *Cdkn2a* expression at both 1 and 6 weeks compared to $CD45^{-}CD31^{-}CD29^{+}$ cells sorted from naïve muscle, suggesting that the stromal compartment represents a significant source of the SnCs in the healing muscle tissue and FBR fibrosis (Fig. 1B, right).

To further investigate which cell types became senescent in the fibrotic capsule, we utilized a SnC reporter mouse strain that we newly generated by homologous recombination in embryonic stem (ES) cells (Fig. 1C, Supplementary Fig. 1A). Like the recently published SnC reporter model [28], this strain drives expression of a tamoxifen-inducible Cre recombinase, $CreER^{T2}$, from the endogenous *p16* gene promoter. However, there are two key differences with the published strain. First, and most importantly, we excised the *neo* gene used for selection of homologous recombinants because it contains enhancer sequences that markedly elevate

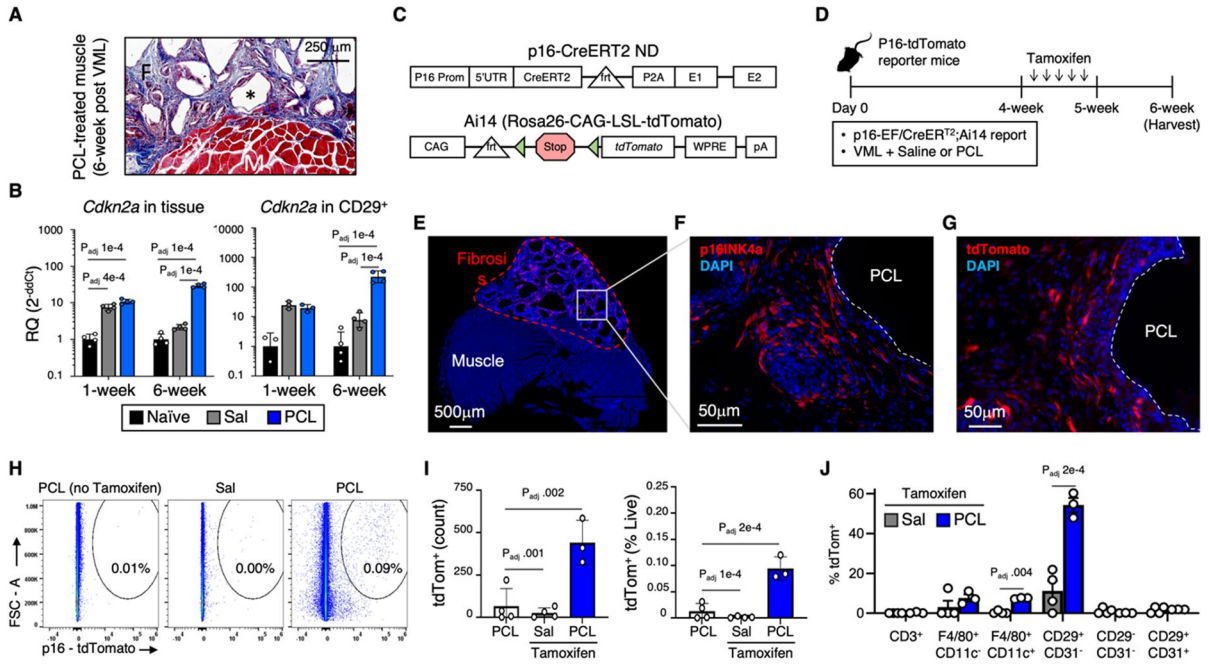

Fig. 1 Cre-transgenic mouse identifies p16^{+} SnCs in fibrotic tissue from the foreign body response to a biomaterial implant. **A** Representative Masson's trichrome staining highlighting fibrosis (F) around PCL particles (*) adjacent to muscle (M) 6 weeks after implantation in a volumetric muscle loss (VML) injury to the quadricep. Scale bar = 250 µm. **B** qPCR analysis of *Cdkn2a* mRNA expression in whole muscle tissue (left) and FACS-isolated CD45^{-}CD31^{-}CD29^{+} cells (right) from naïve/no surgery (black), saline-treated (gray), or PCL-implanted (blue) mice 1 or 6 weeks following VML injury. Statistics shown are from ANOVA followed by multiple *t* test with Benjamini–Hochberg correction for multiple testing. Adjusted *p* values for all statistically significant ($p_{adj} < 0.05$) comparisons are shown. **C** Diagram of the transgene construct used in the *p16-EF/CreER^{T2};Ai14* inducible p16 tdTomato (tdTom) reporter mice. *CreER^{T2}* is inserted inside the *p16*-specific exon 1 of the *Cdkn2a* gene. After tamoxifen administration, Cre recombinase is produced by p16INK4A-expressing cells. Cre then recombines the loxP sites (◄) of the *Ai14* reporter construct resulting in excision of the stop cassette and subsequent functional expression of tdTom. **D** Treatment schematic for the induction of tdTom expression in *p16-EF/CreER^{T2};Ai14* mice. Starting 4 weeks post-surgery, mice received tamoxifen injections daily for 5 days to permanently induce tdTom expression in p16^{+} cells. Tissues were collected and analyzed for tdTom fluorescence 6 weeks post-surgery. **E** Stitched whole cross-section of p16 immunostaining in a WT animal treated with VML surgery and PCL implant (white dashed line), scale bar = 500 µm. **F** Representative image of immunostaining for p16 in a WT animal treated with VML surgery and PCL implants 6 weeks post-surgery, scale bar = 50 µm. **G** Representative image of native tdTom expression in a *p16-EF/CreER^{T2};Ai14* transgenic mouse treated with VML surgery and PCL implants 6 weeks post-surgery, scale bar = 50 µm. **H** Representative flow cytometry pseudocolor dot plots depicting tdTom expression in viable muscle cells from VML-injured mice treated with saline ($n = 4$) or PCL ($n = 3$). Tissues from PCL-treated mice that did not receive tamoxifen injections ($n = 4$) were used to control for background levels of tdTom expression. Population shown was previously gated to remove debris, doublets, and dead cells. **I** Quantification of the tdTom^{+} population in injured muscle by flow cytometry. Total number of viable tdTom^{+} cells is shown on the left and the frequency of tdTom^{+} cells among the total viable population is on the right. **J** Frequency of various cellular subsets within the total tdTom^{+} population in VML-injured animals treated with saline (gray) or PCL (blue). Statistics shown are from multiple *t* test with Benjamini–Hochberg correction for multiple testing comparing saline and PCL within cell types. Adjusted *p* values for all statistically significant ($p_{adj} < 0.05$) comparisons are shown

transcription from the *p16* promoter [29–31]. Second, we incorporated the viral 2A self-cleaving peptide sequence to prevent the complete inactivation of *p16* expression upon insertion of *CreER*^{T2}. To validate the new reporter strain, hereafter referred to as *p16-EF/CreER*^{T2}, we generated heterozygous mouse embryonic fibroblasts (MEFs) and transduced these with an SV40 LT antigen lentivirus, which is known to

activate the endogenous *p16* promoter [32] (Supplementary Fig. 1B). LT antigen indeed induced robust transcription of both *p16* and *CreER*^{T2}. When *p16-EF/CreER*^{T2} cells, expressing a dual fluorescent reporter for CreER^{T2} activity, were exposed to 4-hydroxytamoxifen (OHT), they successfully switched from expressing dsRED to EGFP confirming that *p16-EF/CreER*^{T2}-derived CreER^{T2} was fully functional (Supplementary Fig. 1C–E). Next, we crossed *p16-EF/CreER*^{T2} mice to *Ai14* transgenic mice, which have an LSL-tdTomato reporter construct inserted at the *Gt(ROSA)26Sor* locus and only produce the fluorescent tdTomato (tdTom) protein upon Cre-mediated recombination (Supplementary Fig. 1F). MEFs isolated from *p16-EF/CreER*^{T2}*;Ai14* double heterozygous mice were extensively passaged to induce replicative senescence and then treated with OHT for 1 day prior to analysis (Supplementary Fig. 1G). tdTom^{+} MEFs were observable by fluorescence microscopy with high passage. tdTom^{+} MEFs collected by flow sorting selectively expressed *tdTomato* and had markedly elevated transcript levels of *CreER*^{T2}, *p16*, *p21*, *p19*, and a series of transcripts encoding SASP factors (Supplementary Fig. 1H and I). Additional validation experiments on MEFs from homozygous *p16EF-CreER*^{T2}*;Ai14* mice revealed that small amounts of p16 protein are indeed still expressed via the 2A sequence (Supplementary Fig. 1). These cells underwent senescence after high-dose γ-irradiation as measured by growth arrest and expression of SASP factors *Il6*, *Mmp3*, and *Ccl2* (Supplementary Figs. 2 and 3).

To identify SnCs associated with fibrosis around the biomaterial, we delivered tamoxifen between weeks 4 and 5 post-implantation, after the primary trauma-related senescence resolved (Fig. 1D). At 6 weeks, immunofluorescence (IF) staining reveals p16 staining surrounding the PCL particles, with few to none present in the muscle tissue (Fig. 1E). Higher magnification imaging around the biomaterials shows a high density of p16 staining of cells embedded in the fibrotic region (Fig. 1F). In the transgenic animals, we found cells with tdTom fluorescence in a similar location around the particles with a similar morphology (Fig. 1G and Supplementary Fig. 4). Flow cytometric analysis confirmed that the presence of a PCL implant significantly increased tdTom^{+} cells with few to no cells present in animals not receiving tamoxifen or in saline-treated mice without a biomaterial (Fig. 1H, I). Using a pan immune-stromal flow cytometry panel, we could further determine the cell type that expressed tdTom (Fig. 1J, Supplementary Fig. 5). While less than 0.1% (±0.01% SEM) of cells in the tissue were tdTom^{+}, 54% (±3.6%) of these tdTom^{+} cells were CD45^{-}CD31^{-}CD29^{+} stromal cells. Meanwhile, 15% (±2.1%) of the tdTom^{+} cells were CD45^{+}CD11b^{+} myeloid cells, which were evenly distributed between F4/80^{+}CD11c^{+} scaffold-associated macrophages and F4/80^{+}CD11c^{-} macrophages (7.5 ± 0.2% and 7.6 ± 1.8% of the total tdTom^{+} population, respectively). A small number of myeloid cells expressed tdTom at significantly increased levels; however, we previously demonstrated that sorted CD11b^{+}F4/80^{+} macrophages in this model did not express *Cdkn2a* [22] suggesting that the tdTom signal may be due in part to macrophage engulfment of SnCs or SnC-derived exosomes [22, 33]. Since the majority of the tdTom^{+} cells in the FBR fibrosis were CD45^{-}CD31^{-}CD29^{+} stromal cells, we used this population to generate a senescence gene expression signature.

Angiogenesis and cartilage pathways are activated in tdTom^{+} senescent stromal cells

To identify the phenotype of the stromal tdTom^{+} cells in the FBR, we sorted CD45^{-}CD31^{-}CD29^{+}tdTom^{+} cells and the tdTom^{-} counterpart and performed bulk RNA sequencing. Expression of both the *tdTom* transgene and *Cdkn2a* were elevated in the tdTom/p16^{+} cell population compared to the tdTom/p16^{-} cells confirming that we successfully isolated stromal SnCs (Fig. 2A). Furthermore, the tdTom^{+} cells expressed higher levels of multiple genes associated with senescence including *Mmp13*, *Mmp3*, and *Serpinb2* [34, 35] (Fig. 2B). Surprisingly, we did not observe upregulation of *Il6*, a classic SASP component, in the bulk RNAseq analysis of sorted tdTom^{+} stromal cells. Beyond the recognized SnC genes, broader differential expression identified 1803 genes with increased or decreased expression characteristics in the tdTom^{+} versus tdTom^{-} sorted cell populations (Fig. 2C and Supplementary Table 1, FDR < 0.05).

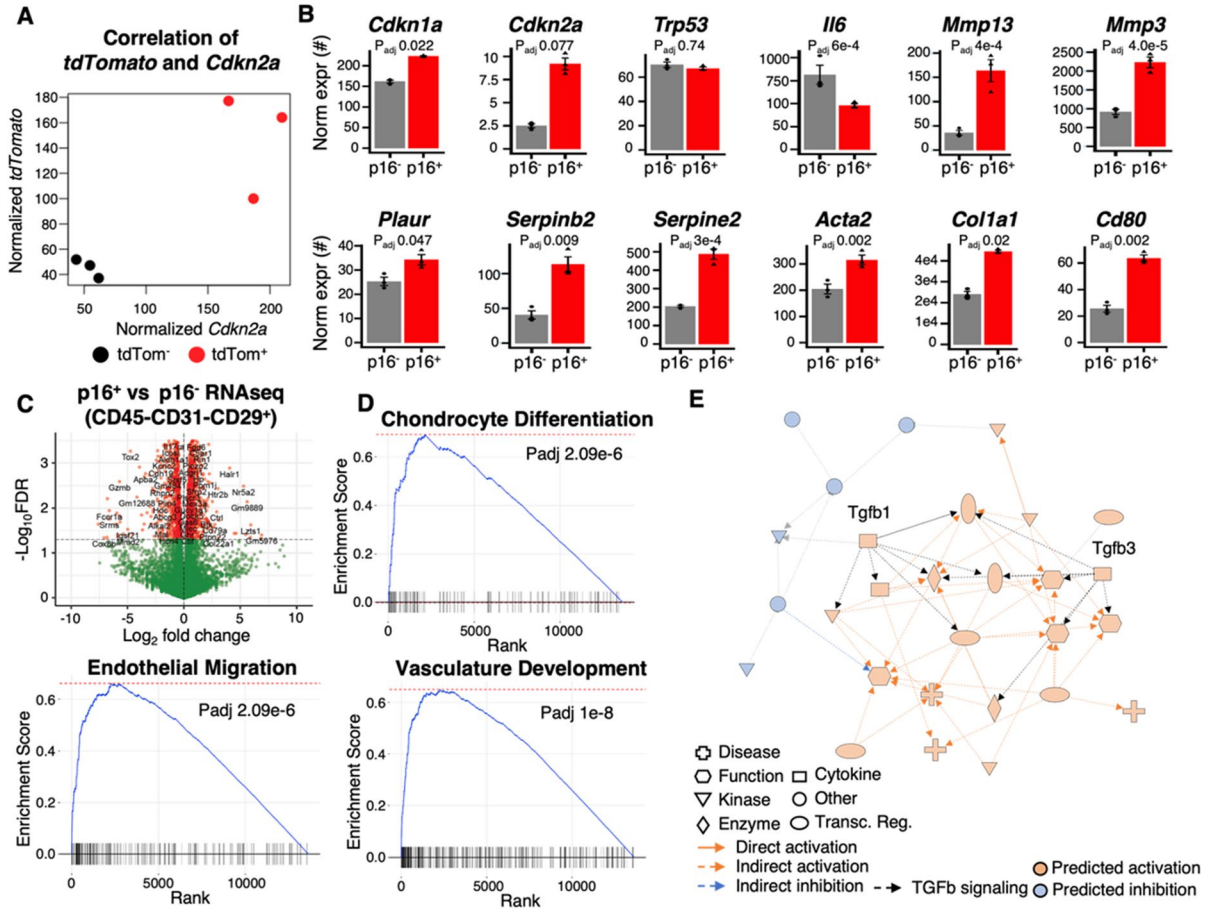

Fig. 2 RNA sequencing identifies a senescence signature from stromal cells in the foreign body response. **A** Gene expression from bulk RNA sequencing comparing sorted $CD45^{-}CD31^{-}CD29^{+}$ $tdTom^{+}$ and $tdTom^{-}$ populations. Correlation of normalized *tdTom* and *Cdkn2a* counts by sample. **B** Normalized gene expression for common senescence-associated genes from the dataset in (**A**). Statistics shown are derived from a negative-binomial test using edgeR followed by FDR correction for multiple testing. **C** Volcano plot depicting differentially expressed genes from the expression comparison in (**A**). Statistics shown are from a negative-binomial test under edgeR with FDR correction for multiple testing. A threshold of 0.05 is used to select significant genes. Positive fold change indicates increased expression in $p16^{+}$ cells. **D** Gene set enrichment analysis (GSEA) for gene ontology biological process annotations. Positive enrichment scores indicate increased expression of the gene set in the $p16^{+}$ cells with increased scores indicating increasingly unlikely enrichment under the assumption of random gene order. Statistics reported are from GSEA with FDR multiple testing correction. **E** Ingenuity Pathways Analysis of upstream regulatory motifs from the bulk RNA sequencing data. The network indicates upstream regulators predicted to be potential modulators of the gene expression changes detected between the $p16^{+}$ and $p16^{-}$ cells in the bulk RNA sequencing. *Tgfb1* and *Tgfb3* transcription factors and their outgoing regulatory connections are indicated in black

To characterize the nature of expression differences in the SnCs versus non-senescent stromal cells, we used gene set enrichment analysis (GSEA) with gene ontology annotations (Fig. 2D, Supplementary Table 2). GSEA identified a number of gene sets associated with either vasculature development or bone/cartilage formation that were upregulated in the $p16^{+}$ stromal populations. Upregulation of cartilage- and bone-related gene sets were driven by extracellular matrix proteins *Col11a1*, *Col20a1*, *Ccn3*, and *Ccn2* as well as growth factors *Tgfb1*, *Bmp2/4/6*, and *Tgfb1*. In contrast, the vasculature-associated gene sets were driven by genes *Myh9*, *Tek*, *Anxa3*, *Sparc*, *Vegfa*, and *Myh9*, all of which are associated with

promotion of vascularization (Supplementary Fig. 6, Supplementary Table 3). These distinct signatures may represent two senescent stromal cell populations in the FBR fibrosis, similar to those previously observed in skin wound healing [23]. Lastly, we used Ingenuity Pathways Analysis (IPA) to probe potential regulatory signatures involved in the senescence phenotype (Fig. 2E). IPA identified transforming growth factor beta (TGFβ) as the primary upstream regulator of the differentially expressed genes in the senescent stromal cells. TGFβ has been widely implicated in mediating fibrosis in multiple pathologies [36–40]. Collectively, our study suggests presence of two heterogenous stromal subsets consisting of vasculature and activated fibroblasts in SnCs and potential role of TGFβ signaling program driving this phenotype.

Single-cell RNA sequencing of stromal cells identifies heterogeneity in the FBR

In order to understand the composition and heterogeneity of the stroma in the FBR fibrosis model, we analyzed the fibroblast portion of our previously published VML scRNAseq atlas [41]. The

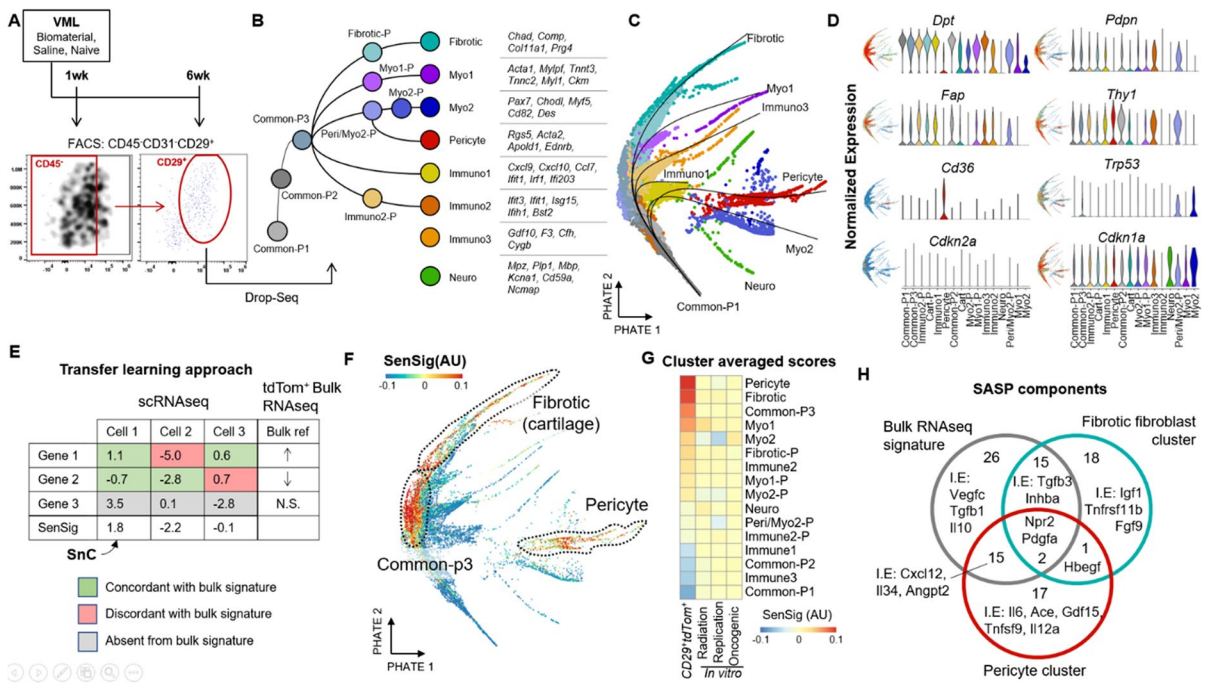

Fig. 3 Transfer learning of senescence signature identifies SnCs in single-cell sequencing of the murine synthetic implant microenvironment. **A** Experimental schema and FACS sorting strategy for single-cell RNA sequencing (scRNAseq). Animals were either uninjured or received the VML surgery that was subsequently treated with either biomaterial implants or saline. $CD45^{-}CD31^{-}CD29^{+}$ cells were sorted 1 and 6 weeks post-surgery before input into the Drop-Seq scRNAseq platform. **B** scRNAseq data set overview. Clusters are labeled and ordered according to their predicted pseudotime trajectory. Characteristic genes for terminal clusters are shown. **C** PHATE dimensional reduction visualization of clusters with psuedotime overlays and terminal clusters labeled. **D** Expression of fibroblast marker genes (top) and senescent markers *Cdkn1a*, *Cdkn2a*, *Trp53*, and *Cd36* (bottom). Both feature plots (left) and violin plots (right) are shown for each gene. The feature plots show the localization of log-normalized gene expression on the PHATE dimensionality reduction scaled from the 0 to 95% percentiles. **E** Transfer learning to identify putative SnC in the scRNAseq data set. A scoring methodology based on *z*-scored gene expression was used to calculate senescent signatures (SenSig) based on the set of genes differentially expressed in the bulk RNA sequencing comparison of sorted SnC in Fig. 2. **F** Calculated SenSig by cells arranged by PHATE. The three clusters with the highest average SenSig are highlighted. **G** Cluster-averaged SenSig derived from the *p16-EF/CreER.^{T2};Ai14* reporter mice as well as from three publicly available senescence signatures from in vitro bulk RNA sequencing. **H** Venn diagram showing differentially expressed ligands (FDR < 0.05) by cluster/data set. Single-cell clusters were compared to all other cells in the data set. Areas with too many genes to show completely have selected genes shown. A complete list of ligands for each category is available in Supplementary Table S5

data was collected with Drop-Seq [42] on sorted $CD45^{-}CD31^{-}CD29^{+}$ cells isolated from wild-type mice with biomaterial implants, control wounds given saline (without an implant), as well as native muscle tissue at 1 and 6 weeks post-surgery (Fig. 3A). The early (1 week) time point and the tissue injury without biomaterial data sets provide information on normal wound healing compared to the later biomaterial implant condition where fibrosis, inflammation, and senescence are enriched. After quality control and thresholding on total UMI count, total feature count, and contribution of mitochondrial genes to total UMI count, the samples were integrated using Harmony [43]. Unsupervised clustering on the resulting combined data set identified 16 distinct stromal clusters characterized by unique gene expression signatures (Fig. 3B, Supplementary Fig. 7A, and Supplementary Table 4).

We first investigated differentiation pathways in the clusters obtained from the scRNASeq analysis. Embedding of cells into a two-dimensional space using PHATE [44], an algorithm based on diffusion mapping which preserves global relationships between cells better than uniform manifold approximation and projection (UMAP) [45], showed multiple branching arms. These arms indicate increasingly differentiated expression states when compared to the other stromal cells, possibly as a result of cellular differentiation (Fig. 3C). CytoTRACE [46], an algorithm which scores scRNAseq data for stemness, identified stem-like clusters which we used in combination with RNA velocity [47] and pseudotime [48] analysis to identify six separate stromal cell differentiation trajectories corresponding to the arms from the PHATE projection (Supplementary Fig. 7B and C). In combination with two cell populations which did not connect via pseudotime with the other subsets, eight terminally differentiated cell populations were identified. The remaining eight clusters of cells were classified as intermediate or progenitor populations along these trajectories. Three of the terminal populations were inflammatory fibroblasts primarily characterized by expression of inflammatory or signaling molecules (Immuno1, Immuno2, and Immuno3). The other five terminally differentiated cell clusters were characterized by genes associated with tissue formation (Fibrotic/Cartilage, Myo1, Myo2, Pericyte, Neuro).

Commonly used fibroblast markers did not appear to resolve the heterogeneity of clusters in our single-cell data set (Fig. 3D). The majority of common fibroblast surface markers like *Thy1*, *Fap*, *Dpt*, *Vim*, and *Pdpn* [19, 49–52] were highly expressed across multiple phenotypically distinct populations, suggesting that traditional fibroblast surface markers are not adequate to resolve the phenotypic diversity seen in the FBR scRNAseq data set. However, we identified vimentin (*Vim*) as a pan-stromal marker and desmopontin (*Dpt*) as a pan-fibroblast marker in our system (Fig. 3D). In addition, we mapped previously collated single-cell atlases [19] of fibroblasts from naïve or perturbed mice to our data set (Supplementary Fig. 8). While most of our clusters mapped to the atlases, many of the distinct phenotypes were pooled more generally. For example, the myogenic, neuro, and pericyte clusters all mapped to stem-like progenitor populations. The majority of the other FBR fibroblast populations mapped to a broad fibroblast cluster defined as adventitia.

The fibrotic cluster from the FBR data set mapped exclusively to an atlas cluster labeled tendon/ligament. To further characterize protein and spatial expression of cartilage-like fibroblast cluster, we performed fluorescent in situ hybridization (FISH) examining expression *Cdkn2a*, *Cd29* (*Itgb1*), and the fibrotic fibroblast cluster marker fibromodulin (*Fmod*) in the PCL implants 6 weeks post-surgery (Supplementary Figs. 9 and 10). We found expression of *Fmod* and *Cdkn2a* exclusively in the fibrosis area surrounding PCL implants and not in healthy tissue, confirming that contaminating tendon or ligament was not responsible for the cartilage-like population.

Despite the known enrichment of $p16^{Ink4a}$-expressing cells in the wound and fibrosis environment determined by qPCR and flow cytometry (Fig. 1), none of the scRNASeq clusters showed distinct expression of senescence-associated genes such as *Cdkn2a*, *Cdkn1a*, or *Trp53*, with the exception of *Cd36* (Fig. 3D), which was the most significantly upregulated gene in the pericyte cluster. Expression of *Cdkn2a* was sparse, likely due to dropout, a phenomenon in scRNAseq where low-expression transcripts are lost. In contrast, expression of *Cdkn1a*, another senescence marker gene, was found across most of the stromal populations in the data set.

Collectively, we reported the stromal heterogeneity in murine foreign body response and identified eight distinct stromal clusters. Via pseudotime trajectory analysis, we identified a common precursor stromal cluster that can give rise to myofibroblasts,

inflammatory fibroblasts, and pericytes. We also identified a myo-pericyte stromal cluster that can potentially give rise to pericytes and myofibroblasts.

Transfer learning with SenSig identifies putative SnC clusters in a murine FBR stromal scRNASeq data set

To identify SnCs in the scRNAseq data set, we developed a transfer learning approach that maps the SnC signature from bulk RNAseq of the transgenic p16 reporter mice to the scRNAseq data set (Fig. 3E). This approach uses a broad set of genes to identify SnC instead of a small number of marker genes, allowing for identification of SnC even if detection of marker genes (like $p16^{ink4a}$) is low or absent. For SenSig generation, we selected the differentially expressed genes from bulk RNAseq of the $tdTom^+$ vs $tdTom^-$ cells (FDR < 0.05) in the scRNASeq data set, identified overlapping genes present in the scRNAseq data set, and lastly sum the *z*-scored expression data by cell weighted by concordance with the direction of the fold change from bulk RNAseq. Genes expressed in a concordant direction increased score while those expressed in a discordant direction decreased the score. The resulting score, which we term SenSig (senescence signature), identifies cells with similar expression patterns to the sorted $p16^+$ cells from the transgenic reporter model. Cells with a high SenSig represent putative SnCs and clusters enriched with high SenSig cells identifies the cellular phenotypes likely enriched for SnCs.

We found the in vivo–derived SenSig primarily identified cells from three clusters in the FBR stromal scRNAseq data set: pericytes, fibrotic fibroblasts, and a common progenitor to both (Fig. 3F). The pericyte cluster was defined primarily by common pericyte marker genes *Rgs5*, *Myh11*, and *Acta2* [53–55]. The fibrotic (cartilage-like) fibroblast cluster was defined by secreted extracellular matrix proteins like *Fmod*, *Chad*, *Comp*, and *Col11a1*, many of which are also expressed by chondrocytes. Three in vitro–derived senescence signatures from the literature [56] (irradiation, replicative, and oncogene-induced senescence) did not map strongly to the scRNAseq cells when compared to our in vivo derived signature (Fig. 3G), suggesting that in vitro–induced senescence does not accurately capture physiological senescence in vivo.

The contribution of genes driving similarity to senescence and a high SenSig can be ranked by cluster (Supplementary Fig. 11). The top SenSig driver genes for the pericyte population were largely associated with vascular function like *Myh11*, *Acta2*, and *Apold1*. Interestingly, *Notch3* was also elevated in the pericyte cluster. *Notch3* has implicated in spatial and transcriptional control of fibroblasts in the synovium of inflammatory arthritis [20]. In contrast, the genes driving SenSig in the fibrotic population were generally extracellular matrix proteins or glycoproteins like *Col11a1*, *Col12a1*, *Thbs4*, and *Ccn2*, the latter of which has been implicated in induction of senescence [57]. This reinforces the association of a senescent, cartilage-like fibroblast population, which we term "fibrotic fibroblasts," that secretes ECM proteins, supported by correlation with tendon and ligament in the fibroblast atlas, and these molecules contribute to pathological fibrosis.

To determine if the transfer learning could identify senescence associated with normal wound healing versus pathological fibrosis, we investigated how SenSig scores varied 1 and 6 weeks post-injury by PCL and compared with saline. During the timecourse of PCL injury, week 1 represents wound healing and week 6 represents pathological fibrosis time points. SenSig high cells were distributed across in both the time points in PCL conditions as compared to saline suggesting SnCs contributing to both normal wound healing and pathological fibrosis (Supplementary Fig. 12).

The SASP is the mechanism by which SnCs impact the tissue environment, so we compared ligands expressed in the bulk RNAseq and scRNASeq clusters (Fig. 3H). We first identified ligands using the CellphoneDB2 [58] database. We determined which ligands increased expression in each high SenSig cluster or in the bulk data set (FDR < 0.05) and then compared the lists of ligands from the three groups. The results showed that while some ligands were common between the bulk signature and each SnC cluster, there were a number of genes that were likely masked due to the combination of cellular phenotypes in the bulk RNA sequencing. Importantly, *Il6*, a well-recognized SASP component that was downregulated in the bulk RNAseq, was upregulated in pericyte cluster but downregulated in fibrotic fibroblasts (Supplementary Fig. 13A and B). This indicates the importance of resolving senescent phenotypes at a cellular level. Because there are distinct SnC phenotypes with

differing expression profiles, bulk RNAseq alone will primarily capture expression patterns that are similar between all of the distinct phenotypes, but may mask important expression patterns that are unique to one of the SnC phenotypes. A complete list of the differentially expressed ligands is available in Supplementary Table 5 and comparison of 1- and 6-week time points is provided in Supplementary Fig. 13C.

Cross-species SnC identification from single-cell RNA sequencing with SenSig

To determine if similar senescent populations were present in human models of the FBR, we collected tissue surrounding surgically excised synthetic breast implants that reproducibly induce fibrosis and demonstrate high levels of SnCs (Fig. 4A). We performed scRNAseq and computationally isolated stromal cells based on expression of *CD29* (*ITGB1*) and absence of *CD45* (*PTPRC*) and *CD31* (*PECAM1*) (Fig. 4B, C). We re-processed the stromal cells to generate six

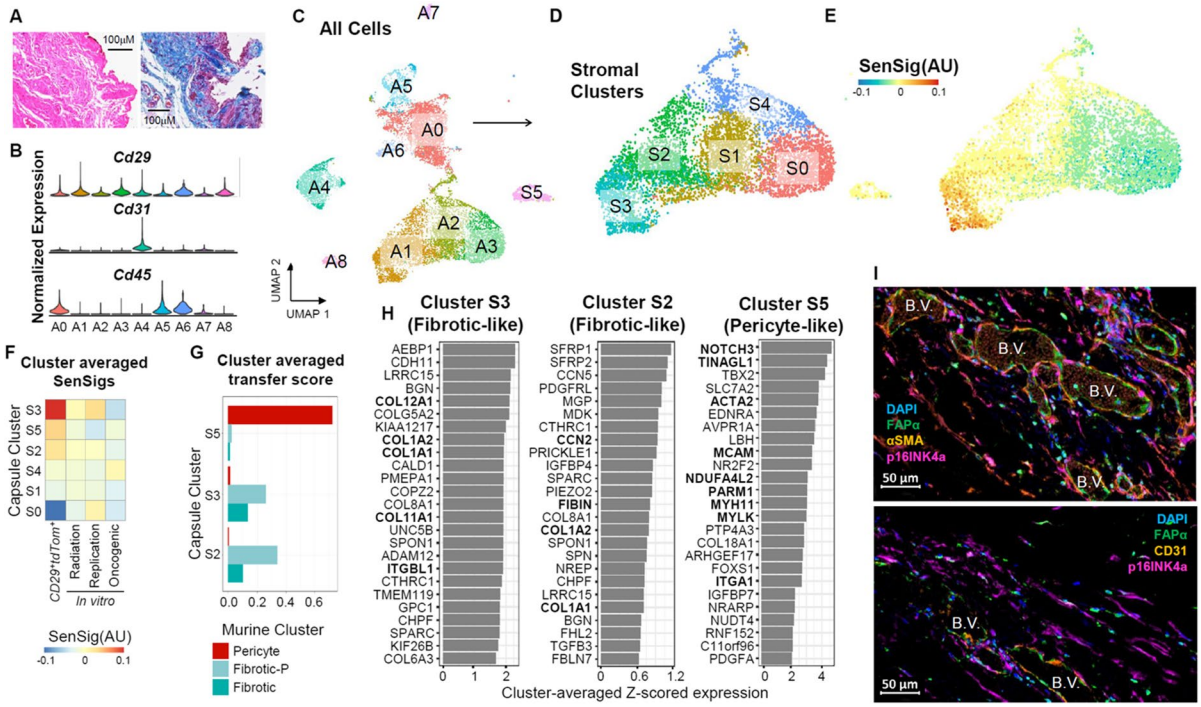

Fig. 4 Mouse to human transfer learning of the senescent signature in single-cell sequencing data set from the fibrotic capsule of a human breast implant. **A** Histological staining of surgically removed fibrotic capsules surrounding synthetic breast implants. Hematoxylin and eosin (left) and Masson's trichrome (right) staining are shown demonstrating fibrosis of the breast capsule tissue, scale bars = 100 μm. **B** Expression of stromal cell markers by cluster from a scRNAseq data set collected from surgically removed synthetic breast implants. $CD45^+$ immune cells were enriched to 50% of the total population prior to scRNAseq library generation using the Drop-Seq protocol. **C** Visualization of the scRNAseq clusters on UMAP before subsetting to stromal populations. **D** Stromal cells from the scRNAseq data set after computational isolate of $CD45^-CD31^-CD29^+$ cells and subsequent re-clustering of the stromal cells. **E** Feature plot visualization of SenSig in stromal cells derived as described in Fig. 3E. **F** SenSig averaged by stromal cluster using our in vivo–derived SnC gene set as well as three publicly available in vitro–derived senescent gene sets. **G** Cluster level similarity scores to the murine putative SnC clusters using singleCellNet. Higher similarity score indicates similar gene expression patterns to the indicated murine scRNAseq clusters. **H** Genes driving the largest increase in SenSig in the three human stromal clusters with the highest average SenSig. Values shown are average *z*-scored expression across cells in the target cluster. Genes that were also in the top 25 genes driving senescent signature in the murine fibrotic or pericyte clusters are shown in bold. **I** Fluorescent staining for fibroblasts (FAPα), endothelial cells (CD31), smooth muscle actin (αSMA), and SnC (p16INK4a) in fibrotic tissue capsules surrounding surgically removed synthetic breast implants, scale bar = 50 μm

stromal clusters and then calculated SenSig by translating the murine gene signature to human equivalent genes based on Ensembl orthologue mapping [59] (Fig. 4D, E).

Three of the six stromal clusters from the human capsule had moderate or elevated SenSig (Fig. 4F). Remarkably, after comparing broad transcriptional signatures of the SenSig high human clusters to the murine stromal clusters, two of these clusters (S2 and S3) shared transcriptional similarities with the murine fibrotic fibroblast cluster and the third cluster (S5) was similar to the murine pericyte cluster (Fig. 4G, Supplementary Fig. 14). Investigation of the genes most responsible for the elevated SenSig by cluster showed distinct modules of genes by cluster (Fig. 4H). The fibrotic, fibroblast-like human clusters were strongly elevated for matricellular proteins *CCN5* and *CCN2*, collagens *COL81A* and *COL1A1*, and *TGFB3*, although interestingly each fibrotic fibroblast-like capsule cluster appeared to have a distinct expression program driving their SenSig respective to each other. The genes driving high SenSig in the human pericyte-like cluster overlapped with numerous genes driving SenSig in the murine pericyte cluster, including *NOTCH3*, *MYH11*, and *MYLK*. In addition, both the fibrotic fibroblast- and pericyte-like clusters shared a number of SenSig driver genes with their respective murine clusters. Most similar driver genes between the human and murine fibrotic fibroblast-like clusters were fibrotic extracellular matrix proteins like *COL1A1*, *COL1A2*, *COL11A1*, and *CCN2* while similar driver genes in the pericyte-like cluster were smooth muscle extracellular matrix proteins like *ACTA2*, *MYH11*, and *MYLK*, although *NOTCH3* was also a top SenSig driver gene.

To validate the presence of SnCs in the fibrotic breast capsule, we performed immunofluorescent staining for $p16^{INK4a}$ in conjunction with stromal (FAPα, αSMA) and endothelial (CD31) cell markers (Fig. 4I, Supplementary Fig. 15). We observed co-staining of αSMA and p16 both adjacent to and distanced from $CD31^+$ blood vessels. Importantly, the majority of p16 positive cells were not FAPα positive, indicating concordance with the scRNAseq data that the senescent populations have low *Fap* expression. These findings suggest that although the SenSig is derived from murine bulk RNA sequencing data, it is sufficient to identify putative SnCs in the human synthetic breast implant fibrotic environment.

SenSig identifies distinct senescent phenotypes in human idiopathic pulmonary fibrosis and cancer

We then sought to determine if our transfer learning approach would identify similar senescent populations in different human pathologies where senescence is thought to play a detrimental role. We used two publicly available data sets of IPF, a disease involving scarring and fibrosis of the lungs independent of any wound or synthetic implant [60, 61] (GSE136831 and GSE135893). Starting from the previously reported clustering from each data set, we calculated SenSig for each data set and determined putative senescent clusters (Fig. 5A, B and Supplementary Fig. 16A, B). In both IPF data sets, we identified similar clusters with high SenSig and distinct phenotypes, including a $KRT5^-/KRT17^+$ cluster, which had previously been proposed to be senescent based on expression of SASP factors and growth arrest [61].

We next compared the IPF clusters with our murine clusters and found that two of the higher SenSig clusters mapped to our fibrotic fibroblast and pericyte clusters in both data sets (Fig. 5C, Supplementary Fig. 16C). The $KRT5^-/KRT17^+$ cluster did not map to our murine data set effectively, indicating that the $KRT5^-/KRT17^+$ population did not have a corresponding cell type in our murine data set. Despite this, SenSig was able to identify this cell population as senescent. This indicates that a cell type–specific compositional bias is not driving elevated SenSig scores but rather that a true conserved SnC phenotype is present and is sufficient to identify senescence in new cell types that were not a part of the bulk senescence sequencing.

Finally, we investigate the genes driving the elevated SenSig in the top 3 clusters from each data set (Fig. 5D, Supplementary Fig. 16D). The pericyte-like clusters shared SenSig driver genes with their respective murine cluster. However, the myofibroblast clusters and the two top-scoring SenSig clusters had distinct SenSig driver genes which did not overlap with murine clusters. The absence of overlap in SenSig driver genes between the IPF myofibroblast and murine fibrotic clusters suggests that although they share some similar transcriptional signatures, there may be distinct SnC programs in these populations. Furthermore, the identification of the aberrant basaloid and KRT5 − /KRT7 + clusters as senescent, neither of which mapped to any murine clusters, suggests that although our gene signature is derived from foreign body response to a synthetic implant, it can be

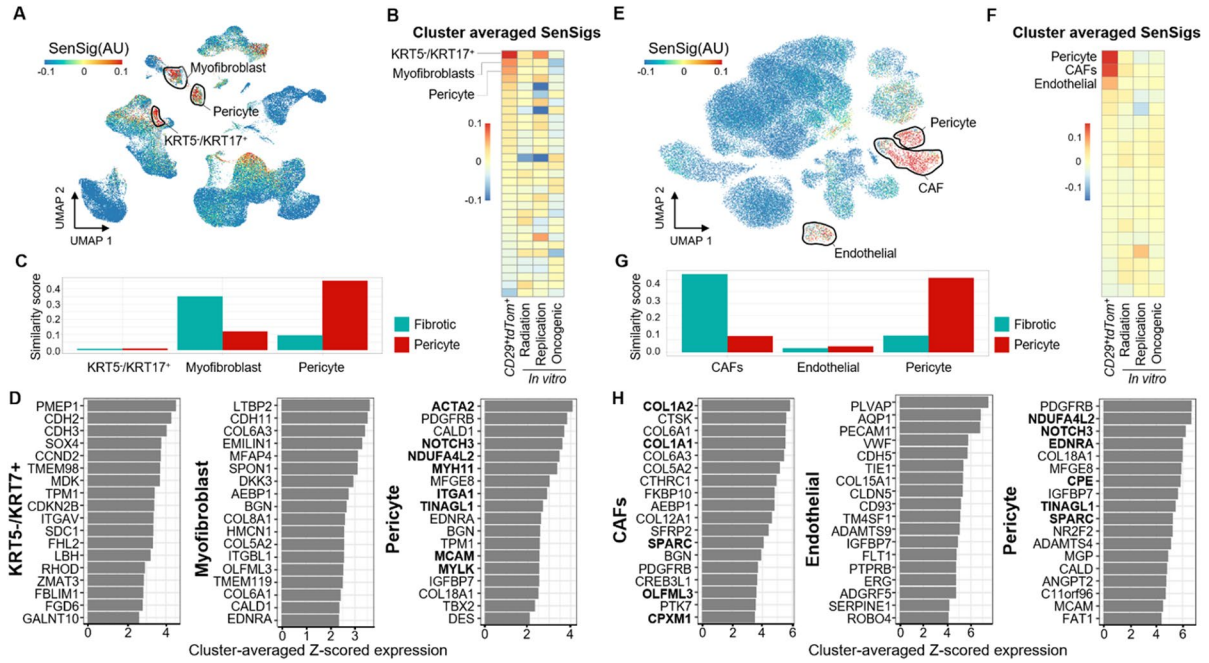

Fig. 5 SenSig identification of SnC in diverse tissue microenvironments. Putative senescent characteristics of two publicly available scRNAseq data sets from human samples of idiopathic pulmonary fibrosis (IPF) (left) and basal cell carcinoma (BCC) (right). **A**, **E** Feature plots of SenSig calculated as described in Fig. 3E. **B**, **F** Cluster averages of SenSig using our in vivo–derived senescence signature as well as three in vitro–derived publicly available gene sets. Clustering included in the publicly available data were used and are described in detail in their respective publications. **C**, **G** Similarity scores using our murine, VML-derived scRNAseq clusters as references. Higher similarity scores indicate similar gene expression patterns to murine scRNAseq stromal clusters. **D**, **H** Genes driving the largest increase in SenSig in the three human stromal clusters with highest average SenSig. Values shown are average *z*-scored expression across cells in the target cluster. Genes that were also in the top 25 genes driving senescent signature in the murine fibrotic or pericyte clusters are shown in bold

successful in identifying SnC in broader contexts and cell types beyond a pericyte and fibroblast.

We then applied the same analysis technique to a publicly available data set of basal cell carcinoma (BCC) [62]. Using the authors' cluster annotations, we identified three clusters with elevated SenSig: pericytes, cancer-associated fibroblasts (CAFs), and endothelial cells (Fig. 5E, F). The CAFs and pericytes mapped to our fibrotic and pericyte murine clusters respectively and, unsurprisingly, the endothelial cell population was not similar to either (Fig. 5G). Finally, examination of the driver genes within each cluster identified a number of fibrotic genes driving SenSig in the CAFs and a number of genes associated with smooth muscle formation in the pericytes as well as *NOTCH3* (Fig. 5H). While the IPF-derived myofibroblast population did not have any overlap in driver genes with our murine fibrotic population, the cancer-derived CAFs shared a handful of common driver genes (*COL1A1*, *COL1A2*, *SPARC*, *OLFML3*, and *CPXM1*). The CAFs also had a higher similarity score to our fibrotic population than the myofibroblasts. Together, these findings suggest that our fibrotic population is more similar to CAFs than the myofibroblasts derived from the IPF environment. The endothelial cell population had a number of traditional endothelial cell markers as driver genes (*VWF*, *PECAM1*, *TIE1*), none of which overlapped with either the fibrotic or pericyte SenSig driver genes. The identification of a SnC phenotype distinct from the reference data suggests that the transfer learning technique is generalizable to both new microenvironments and at least some new cellular phenotypes.

Transfer learning identifies conserved and tissue-specific SASP factors

Identification of SnCs across multiple tissues and pathologies provides the opportunity to explore

SASPs that may be conserved and tissue specific. Similar to the ligand identification in the bulk SnC gene set, we determined differentially expressed ligands in the clusters with high SenSig using the CellphoneDB2 [58] database across the wound, fibrotic breast capsule, IPF, and BCC (Supplementary Fig. 17). To match the murine VML-derived ligands with the other human data sets, we used Ensembl orthologue mapping to translate genes from MGI to HGNC symbol. It is important to note that this species translation combined with differences in scRNAseq chemistry (Drop-Seq vs. 10X genomics) and number of cells collected across the data sets may cause false identification of microenvironment-specific ligands. Identification of ligands across environments represents a conserved effector process by which the distinct SnC populations are functionally affecting their environment.

We identified *IL6*, a classical SASP factor, in the conserved pericyte SASP factors found in all conditions (Fig. 6A). Interestingly, *IL6* is associated with both inflammation and angiogenesis. In wound healing, *IL6* promotes stemness and stimulates proliferation, migration, and vessel formation in endothelial progenitor cells. Circulating *IL6* levels increase with exercise, highlighting the beneficial roles of *IL6* in

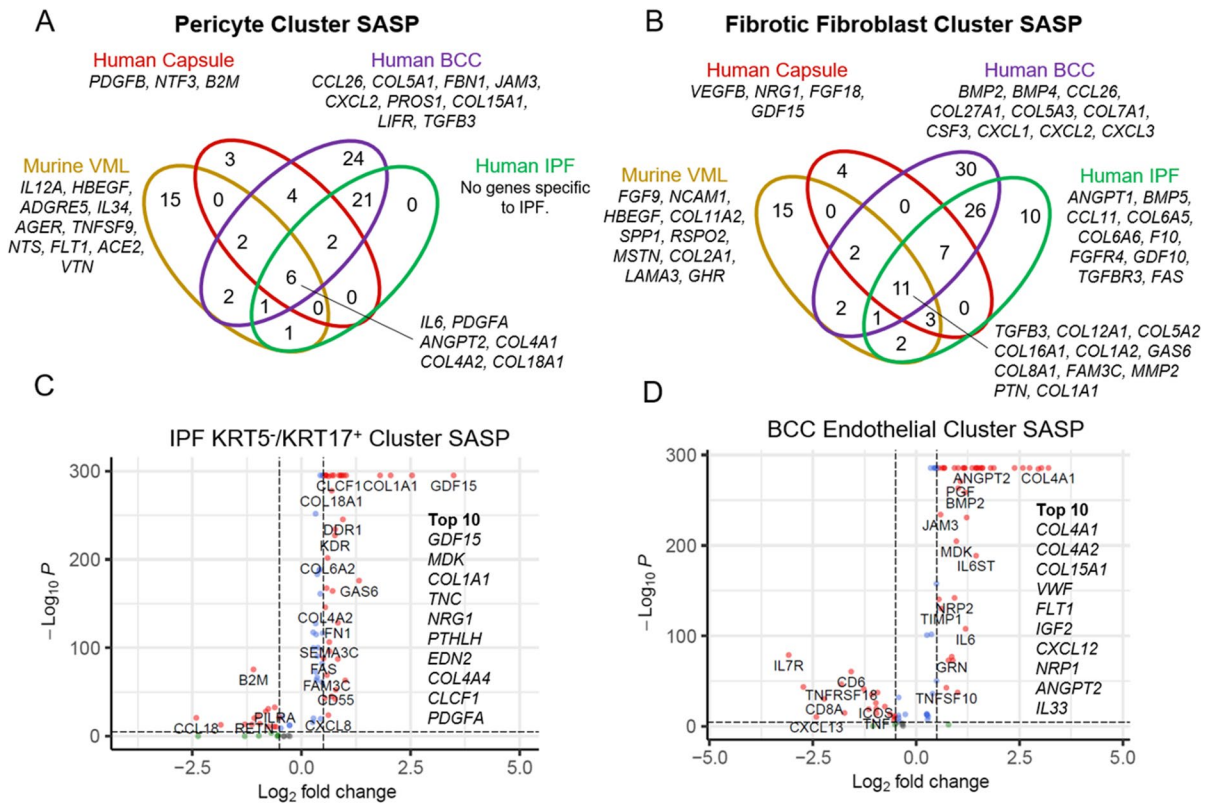

Fig. 6 Expression of ligands by corresponding SnC clusters across tissue microenvironments. **A** Venn diagram showing differentially expressed ligands (FDR < 0.05) in the SenSig high pericyte clusters and **B** SenSig high fibrotic fibroblast clusters in the VML, human breast capsule, BCC, and IPF data sets. Ligands were selected from the CellphoneDB2 data base. Murine genes from the VML data set were converted from MGI to HGNC symbol using Ensembl orthologue mapping. Each cluster was compared to all other cells in its respective data set by Wilcox rank sum followed by Benjamini–Hochberg correction for multiple testing. Sets of genes that were specific to each cluster are shown as well as genes that were common across all data sets. A complete list of ligands for each cluster present is available in Supplementary Table S5. **C** Volcano plots of differentially expressed genes for the KRT5^{-}/KRT17^{+} epithelial-derived basaloid cluster from the IPF data set and **D** the endothelial cell cluster from the BCC data set. Ligands were selected from the CellphoneDB2 database. *P* values shown are from Wilcox rank sum comparing each cluster with all other cells in the data set followed by Benjamini–Hochberg correction for multiple testing

tissue healing. On the other hand, *IL6* is also correlated with dysfunctional angiogenesis and inflammation in disease pathology. While bulk sequencing of the fibroblasts identified a decrease in *IL6* expression, we also found that different subsets of fibroblasts up- or downregulated *IL6*. This heterogeneous *IL6* expression is likely why we see lower expression of *IL6* in bulk tissue but also identify it as an important component of communication with the pericytes. Additional conserved SASP factors in the pericytes include *COL4*, a component of the basement required for new vessel development, and *COL18*, a negative regulator of cell proliferation and matrix-dependent angiogenic processes. Finally, there was conserved expression of the angiogenesis-related growth factors platelet-derived growth factor (*PGDF*) and angiopoietin 2 (*ANGPT2*) which are both found during normal tissue development and contributing to pathological inflammation.

There were 11 conserved fibrotic fibroblast SASP factors that were present in all of the conditions and associated with matrix production including multiple forms of collagen (Fig. 6B). For example, *FAM3C* is a stimulator and metabolic regulator of epithelial–mesenchymal transition (EMT) and *TGFB3* has long been associated with fibrosis. Interestingly, pleiotrophin (*PTN*) is a heparin binding cytokine that functions downstream of PDGF. Tissue-specific fibrotic SASP factors include collagen types along with growth factors and cytokines unique to each condition, again highlighting both conserved and context-dependent SASP production. The cell types that were unique to IPF and cancer, the KRT5^{-}/KRT17^{+} and endothelial cells, respectively, expressed SASP factors that were found in both the pericyte and fibrotic high SenSig clusters suggesting dysfunctional angiogenesis and matrix production/fibrosis (Fig. 6C, D).

Senescent pericytes activate myeloid cells through IL34 signaling in wound healing

To determine intercellular signaling patterns between SnC and other cells in the microenvironment, we analyzed the CD45^{+}-enriched portion of our previously published VML scRNAseq atlas [41]. The data set was collected in VML treated mice 1 week post-injury with enrichment of CD45^{+} cells to ~ 50% of the total cell population (Fig. 7A). After computationally identifying immune cell populations as well as the CD31^{-}CD45^{-}CD29^{+} stromal populations, we used singleCellNet [63] to label stromal cells in the CD45^{+}-enriched data set with our previous cluster labels (Fig. 7B). The resulting data set contains both immune clusters as well as stromal clusters corresponding to what we described in Fig. 3. We then used Domino [41] to identify any potential signaling between the SnC enriched and myeloid clusters. Domino is an algorithm which predicts intercellular signaling patterns by first identifying activated transcription factors within each cell and then finding receptors with correlated expression to the activated transcription factors. Finally, if corresponding ligand expression is captured by scRNAseq, the cluster expression is used to identify intercluster signaling. The results are a global signaling network connecting transcription factors activated in the data set with their correlated receptors and, if detectable, ligands which could potentially activate the receptors. By selecting transcription factors enriched in a target cell population, it is possible to identify signaling directed at that population, for example targeting the myeloid or fibrotic clusters (Fig. 7C and Supplementary Fig. 18).

Domino identified two major signaling pathways between SnC enriched and myeloid populations. First, it predicted *IL34* from the SenSig high pericyte cluster would activate myeloid populations through *Csf1r* and ultimately activation of transcription factors *Bcl11a* and *Gli1* (Fig. 7D). Importantly, *Il34* was one of the genes detected both in the bulk RNA sequencing senescent signature as well as upregulated in the pericyte scRNAseq cluster. It also predicted that *Tgfb1* and *Il11* would target the fibrotic fibroblast population of SnCs and ultimately lead to fibrosis through activation of transcription factors *Glis1* and *Six1*, respectively, both of which have been implicated in fibrosis [64, 65] (Fig. 7E). The myeloid populations expressed the highest levels of *Tgfb*, although *Il11* was not detected in our single-cell data set. Together, these findings suggest signaling from pericytes influences differentiation of myeloid populations which, in turn, secrete molecules affecting the fibrosis by fibrotic populations (Fig. 8A).

To validate Domino's findings, we first sought to determine whether senescent and myeloid cells were adjacent to each other in the fibrotic microenvironment in vivo. Both FISH staining for *Cd45*

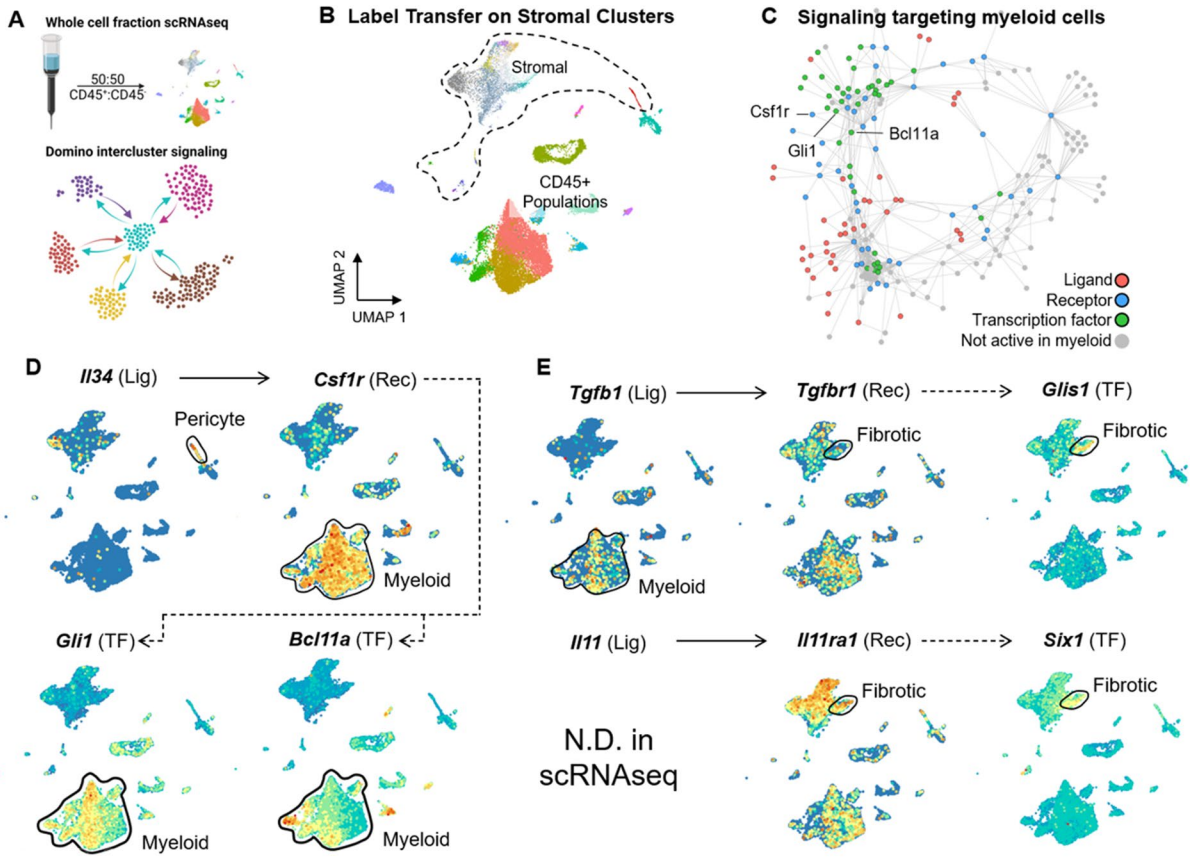

Fig. 7 Intercellular signaling patterns involving SnC. **A** Summary of methodology to obtain intercluster signaling patterns. A whole-cell fraction scRNAseq data set from mice treated with VML with saline, biomaterial implants, or naïve animals was obtained 1 week after surgery with enrichment of $CD45^+$ cells using MACS beads. After mapping stromal clusters to the data set, Domino was used to calculate intercluster signaling patterns. **B** Visualization of stromal and non-stromal clusters within the whole-cell fraction scRNAseq data set. Stromal clusters are colored as in the stromal scRNAseq data set shown in Fig. 3. **C** Signaling predicted to be actively targeting myeloid cells. **D** Feature plots of components of signaling pathways predicted to be active from pericytes targeting myeloid cells and **E** from myeloid cells targeting fibrotic fibroblasts. Solid lines represent ligands capable of activating receptors in the CellphoneDB2 database and dotted lines represent correlation between transcription factors and receptors

(*Ptprc*) and *Cdkn2a* and immunofluorescent staining for $p16^{INK4a}$ and F4/80, a macrophage marker, showed colocalization of immune/myeloid cells and SnC in mice treated with PCL implants (Fig. 8B, Supplementary Fig. 19). Immunofluorescent staining for p16, endothelial cell marker CD31, and macrophage marker CD68 in human fibrotic breast implant samples further demonstrated close proximity of senescent pericytes and fibrotic cells adjacent to macrophages, suggesting possible interactions and communication in murine and human fibrotic environments (Supplementary Fig. 20).

To further validate the computationally predicted interactions, we ran bulk RNA sequencing on senescent and quiescent murine stromal cells induced by irradiation and low-serum media, respectively, as well as macrophages alone or co-cultured with senescent stromal cells in vitro. Aligning with Domino's prediction, we found elevated expression of *Il34* in senescent stromal cells compared to quiescent stromal cells as well as increased expression of *Csf1r*, the receptor for *Il34*, *Tgfb1*, and type 1 inflammatory cytokine *Il1b* in the macrophages co-cultured with SnCs (Fig. 8C). These results suggest that senescent stromal cells have elevated *Il34* and that upon co-culture with SnCs,

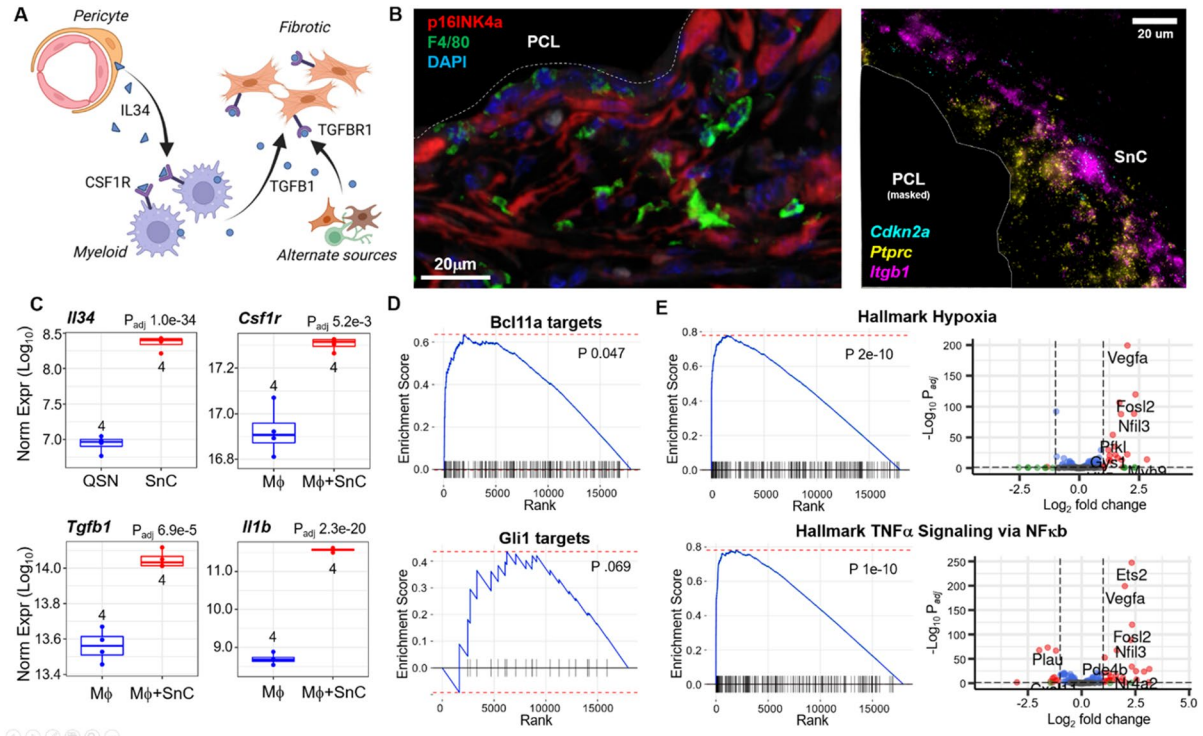

Fig. 8 Validation of Domino-predicted intercellular signaling patterns. **A** A graphical representation of signaling pathways involving the pericyte and fibrotic senescent populations predicted by Domino. In the PCL microenvironment, pericytes express IL34 binding to and activating CSF1R on myeloid cells. The myeloid cells further express TGFB1 which induces fibrosis in fibrotic SnCs through TGFBR1. **B** Immunofluorescent staining of p16.^{INK4a} and macrophage marker F4/80 near the PCL implant (left). FISH staining for immune cell marker CD45 (*Ptprc*; yellow), stromal cell marker CD29 (*Itgb1*; pink), and p16 (*Cdkn2a*; blue) near the PCL implant (right). Both images are representative of animals treated with PCL implants 6 weeks post-surgery, scale bar = 20 μm. **C** Gene expression of select transcripts predicted to be involved in signaling between senescent pericytes and macrophages after co-culture of senescent stromal cells with macrophages. Gene expression of *Il34* is compared between quiescent (QSN) and SnC stromal cells while other genes are shown in macrophages cultured alone or with SnC stromal cells in transwell plates. **D** Gene set enrichment for the Domino-predicted Bcl11a and Gli1 target genes in macrophages cultured with SnC compared to cultured alone. Positive enrichment indicates overexpression of the module of genes predicted to be targeted by each transcription factor in macrophages co-cultured with SnC. **E** Gene set enrichment for Hallmark Hypoxia and TNFα signaling gene sets in macrophages cultured with SnC compared to cultured alone (left). Positive enrichment indicates overexpression of the module of genes predicted to be targeted by each transcription factor in macrophages co-cultured with SnC. Volcano plots showing fold change and statistical significance of each gene in the gene sets are also shown (right)

macrophages increase expression of *Csf1r*, begin to secrete elevated levels of *Tgf1b*, and obtain an inflammatory phenotype as marked by increased expression of *Il1b*. GSEA identified statistically significant overrepresentation of the Bcl11a and Gli1 targets predicted by Domino, suggesting that co-culture of macrophage with *Il34*-expressing SnC led to the changes in gene expression predicted by Domino (Fig. 8D). Finally, GSEA with the Hallmark gene sets identified overrepresentation of genes associated with hypoxia, angiogenesis, ECM–receptor interactions, and TNFα signaling in macrophages co-cultured with SnC, confirming an inflammatory response in the co-cultured macrophages (Fig. 8E, Supplementary Fig. 21).

Discussion

The field of senescence has grown significantly over recent years as the association of senescence and multiple age-related pathologies has been elucidated. However, the question of senescent cell

identity, heterogeneity, and ultimately function remains unknown. New transgenic models are enabling better visualization and identification of the rare cells expressing p16; however, the phenotypic understanding of SnCs is limited due to the challenges in isolating these cells. Model systems that can enrich p16 expressing cells enable the isolation of adequate cell numbers for in-depth phenotypic analysis. Fibrosis induced by the biomaterial foreign body response provides a reproducible system for SnC enrichment where p16 expressing cells can be readily identified, their phenotype characterized, and specific senescent cell populations can be isolated. Bulk RNA sequencing of stromal $CD45^{-}CD31^{-}CD29^{+}$ SnCs captured 17,638 RNA transcripts after quality control filtering compared to the 6751 transcripts expressed in more than 5% of cells in our single-cell RNA sequencing data set. The relatively low transcript abundance in scRNAseq makes it difficult to identify SnC with transcripts like *Cdkn2a*, the transcript encoding p16, too low to detect by microfluidic-based scRNAseq techniques. The resulting differential expression profile represents the first direct, physiologically relevant, in vivo senescent gene expression signature.

Our SenSig transfer learning method provides a robust method to identify SnCs across tissues, species, and pathologies. Transfer learning in the context of scRNAseq refers to techniques which leverage existing or higher-fidelity data sets to identify similar cell populations across data sets [25]. Importantly, these techniques can leverage gene expression patterns across hundreds or thousands of genes to overcome the inherently low transcript capture rates in scRNAseq. Here, we showed how the murine FBR-induced fibrosis senescence signature could be used to identify SnCs in the human foreign body response, idiopathic pulmonary fibrosis, and the tumor microenvironment. The SenSig approach identifies conserved properties of senescence while at the same time providing tissue-specific and pathology-specific context allowing for examination of specific genes driving the elevated signature within each cluster or even within each cell. Identification of senescent epithelial-derived basaloid cells in IPF highlights the power of SenSig to capture conserved elements of senescence within tissue-specific cellular phenotypes not present in the reference data set. Moreover, publicly available senescence signatures derived from in vitro models did not lead to identification of senescent populations in any of the in vivo single-cell data sets where there are known SnCs. This suggests that the in vitro models of senescence (oxidative, oncogenic, and proliferative) do not necessarily recapitulate physiologically relevant senescence in many pathologies. Other mechanisms of senescence, particularly immunologically induced senescence [3], may provide new insights into physiologically relevant function that can be modeled in vitro.

One of the paradoxes of the senescence field is the beneficial contribution of SnCs during development and wound healing and the pathological influences in age-related diseases. Possible explanations suggest the existence of "good" versus "bad" SnCs with different phenotypes or kinetics of senescence that contribute to tissue development or pathology. GSEA of the SnC expression profile identified two distinct pathways related to angiogenesis/vascularization and cartilage. The angiogenesis connection of SnCs was first identified by Demaria et al. in skin wounds where PDGF-BB could reconstitute SnC functions in tissue healing [23]. The presence of p16 expressing cells surrounding blood vessels visualized by immunofluorescence and the pericyte single-cell cluster expressing the strongest SenSig further support the angiogenic contributions of SnCs and suggest that this population could be considered a beneficial senescent cell at least in the context of wound healing.

The annotation of the cluster with the second highest SenSig was first classified as cartilage due to the large number of associated extracellular matrix molecules. FISH staining for the cluster-associated gene *Fmod* confirmed that the cells were in the regions of fibrosis and not contaminating tendon or ligament cells from the surrounding muscle. Fibrosis is, however, characterized by a thick, often aligned, extracellular matrix (ECM) similar to cartilage and tendon tissues. Many ECM proteins that are expressed by cells in the fibrotic region of the FBR are also found in cartilage including *Acan*, *Cilp*, *Chad*, and *Comp* [66]. While tissue-specific properties of fibrosis occur, it appears that fibrosis recapitulates aspects of native tendon and cartilage tissue structure to create a barrier tissue with dense, avascular, organized, and frequently aligned extracellular matrix. Particularly with the correlation of senescence with dysregulated tissue function and pathological fibrosis, this unique senescent population provides a potentially new therapeutic target.

Interestingly, *CCN2* and *CCN5* were elevated in the senescent fibrotic fibroblast clusters as well as in the sorted tdTom$^+$ SnC. The CCN matricellular proteins have been implicated in induction of senescence in a variety of contexts [57, 67, 68]. They are also regulatory targets of the YAP/TAZ pathway, a mechanosensing pathway recently highlighted for its potential role in fibrosis [69–71]. Activation of YAP was associated with increased fibrosis, increased expression of CSF1 leading to myeloid-derived inflammation, and increased expression of CCN family members. Taken together with our findings, we hypothesize that induction of YAP associated with tissue damage-associated mechanical changes may induce senescence through secretion of matricellular CCN family members that subsequently activate myeloid cells, a process that is important for wound healing but that can also result in fibrosis.

While p16 is one of the primary markers used to identify SnCs and multiple transgenic mouse models have been developed to specifically monitor and clear *p16* expressing cells to extrapolate function, it has long been questioned as a definitive marker of senescence. For example, Dieckman et al. showed that p16 expression correlated with senescence, but it was not a driver of senescence since inducing p16 expression did not lead to production of a SASP [72]. The senescent expression signature we present here was generated from p16 expressing cells, but since it creates a signature of many genes that are increased and decreased, it can be used to identify cells with similar expression changes regardless of p16 expression. This is demonstrated by the identification of senescent clusters in the single-cell data sets where p16 expression is not captured and p21 expression, another marker of senescence, is expressed across multiple subsets. Cell-intrinsic or -extrinsic environmental factors may be responsible for the variable expression and need for p16 expression to arrest cell growth. Terminally differentiated cells such as those expressing many ECM molecules have limited replicative capacity and the dense fibrotic ECM in which the cells are embedded may reduce the need for cyclin-dependent kinase inhibitors for growth arrest compared to cells such as pericytes active in angiogenesis. However, the fibrotic nature of the cartilage-like SnCs suggests these cells may be more associated with pathology rather than wound healing or potential beneficial effects of the angiogenic pericytes.

While fibroblasts were previously considered a supporting cell type, the complexity of fibroblast populations and their significant roles in multiple diseases and aging is now being elucidated. Single-cell technologies opened the door to characterizing fibroblast heterogeneity and function while also providing markers for classification. Because p16 expression is not captured in scRNAseq data sets as mentioned previously, SnCs are not identified in the fibroblast or stromal single-cell clusters in most data sets even though multiple studies identified fibroblasts as a cell type that becomes senescent [22, 23]. Moreover, expression patterns and immunofluorescence of well-accepted fibroblast markers, including Thy1.1, FAP, PDPN, and αSMA, do not distinguish senescent fibroblasts. The SenSig transfer learning approach contributes to senescence and fibroblast advances by identifying which subsets of fibroblasts exhibit high senescence signatures and distinguishing senescence heterogeneity with elucidation of distinct senescent fibroblast subsets.

Senescent cells may be a key player in immune-stromal interactions that are critical for tissue homeostasis and repair. Inflammatory fibroblasts and SnCs expressing a SASP produce immunologically relevant cytokines that support robust stromal communication with the immune system. We previously demonstrated a connection between SnCs and the immune environment in the foreign body response and osteoarthritis [22]. In these models, there was a feedforward reinforcement between type 3 immune immunity characterized by Il17 production and senescence with an inflammatory-induced senescence signature identified in vitro. Of note, this is not immunosenescence but the impact of SnCs on the migration, activation, and regulation of immune cell phenotype. T Cells are intimately connected to the innate immune system and often drive myeloid skewing and macrophage phenotype and thus are likely connected, directly or indirectly with SnC behavior. Applying cell–cell communication analysis to a single-cell data set where the SnCs are identified by transfer learning, we were able to predict the unique myeloid communication with pericyte and fibrotic fibroblast populations that contributes to the balance of tissue vascularity and matrix production. The first prediction of senescent pericytes activating transcription factor programs in myeloid cells suggests coordinated stromal-immune activity

in angiogenesis. Pericytes are well recognized as progenitor cells that can contribute to angiogenesis, but myeloid cells also promote vascular development through production of VEGF as demonstrated in the FBR [73–75]. A different set of myeloid cells expressed ligands that activated TFs in the fibrotic SnCs suggesting that the immune system contributes to pathological SnC activation and fibrosis.

There remains the fundamental question of what is a SnC. To this end, multiple approaches are being explored to derive senescent signatures. Early attempts to derive a senescent signature focused on sequencing SnCs cultured in vitro. While these in vitro studies allowed controlled conditions to evaluate oncogenic, proliferative, and radiation-induced senescence, it is unclear how much they represent physiological senescence. However, identification of genes expressed across these multiple types of SnCs provides a potential conserved signature that may be broadly applicable [56]. Casella et al. also derived a senescence signature from in vitro culture with a smaller set of conserved genes across senescence types [76]. More recently, Saul et al. developed the SenMayo senescence signature by curating a gene set from an extensive literature review [77]. While the SenSig transfer learning method depends on isolation of p16-expressing cells, a controversial senescence marker that may only be correlative [72], it generates a large gene set of up- and downregulated genes to create a broader profile that can capture senescence similarities across diverse conditions. Moreover, the transfer learning method identifies SnC similarities independent of p16 expression.

While we developed a potentially broadly applicable senescence signature, the specific molecular characteristics of the SnCs we identify are not fully explored. We predicted intercellular signaling with Domino and validate both the SenSig and intercellular signaling with orthogonal biological experiments but do not investigate specific mechanisms of signaling. Despite our knowledge that in vitro senescence is not the same as that found in vivo, there are few options to generate adequate SnC numbers to conduct in vitro studies to validate intercellular communication. In vivo studies that enable selective deletion of the SnC subtypes will be able to further validate the predicted SnC phenotype and SASP impact on the local environment. Finally, Domino does not use SenSig directly but rather the clusters that are enriched for SnC to predict communication. Future studies will be able to further elucidate SnC phenotype and function as signatures continue to be refined and computational and murine model tools are developed.

Methods

Animal welfare statement

All animal procedures were performed in adherence to approved JHU IACUC protocols.

Volumetric muscle loss surgery and biomaterial implantation

All volumetric muscle loss surgeries were performed when animals were at least 10 weeks of age. Bilateral muscle resections of the quadriceps were performed as previously described. Defects were filled with 30 mg of (poly)caprolactone (particulate, Mn = 50,000 g/mol, mean particle size < 600 μm; Polysciences), decellularized extracellular matrix (Matristem; Acell), or 50 μL of phosphate-buffered saline as a control. All materials were UV sterilized prior to implantation and all animals given subcutaneous carprofen (Rimadyl Zoetis) at 5 mg/kg. Samples were harvested 1 or 6 weeks post-surgery. During harvest, the complete quadriceps together with any remaining implant material was harvested and processed for downstream experiments as described in the following sections.

Clinical samples

Deidentified surgical discards from patients undergoing breast implant exchange or replacement surgeries were collected under Johns Hopkins University Institutional Review Board exemption IRB00088842. After collection, the samples were processed for downstream experiments as described in the following sections.

Generation of the p16-EF/CreER^{T2} mouse strain

A targeting construct containing 5′ and 3′ *p16* homology arms of 1.2 and 1.3 kb, respectively, were amplified from TL1 ES cell genomic DNA. Fragments

containing CreER^{T2}-FRT and PGK-NEO-FRT-P2A were derived from pCAG-CreER^{T2} (Addgene, Plasmid #14,797) and PL451, respectively. The P2A sequence used was GCTACTAACTTCAGCCTGCTG AAGCAGGCTGGAGACGTGGAGGAGAA CCC TGGACCT [78]. CreER^{T2}-FRT-PGK-Neo-FRT-P2A sequences were inserted between the homology arms and then cloned into pDTA.4B. The resulting targeting vector and TALEN plasmids for enhanced homologous recombination were electroporated into TL1 ES cells and G418-resistant clones were screened by Southern blot analysis of *HindIII* digested DNA using a 497-bp genomic *p16* gene fragment upstream of the 5′ arm as a probe. Correctly targeted ES clones were injected into C57BL6/NHsd blastocysts to obtain chimeric mice, and then the chimeric mice were bred with C57BL/6NHsd mice (Envigo). The germline transmitted F1 heterozygote mice were then crossed with *FLP* transgenic mice (Jackson laboratory, #003,946) to excise the *PGK-NEO* gene cassette. Two weeks prior to collection of tissue from reporter mice, five intraperitoneal injections of tamoxifen solubilized in corn oil (14 mg/mL) were administered daily at 70 mg/kg/day.

MEF isolation and culture

Mouse embryonic fibroblasts (MEFs) were generated from embryonic day E13.5 embryos as described previously. *P16* knockout cells were described previously [79]. Cells were expanded in DMEM (Gibco, #11,960) supplemented with 10% heat-inactivated fetal bovine serum, L-glutamine, non-essential amino-acids, sodium pyruvate, gentamicin, and β-mercaptoethanol. At cell passage 3, cells were harvested "d0 non-senescent" or subconfluent cell layers (60–80% confluence) were subjected to 10 Gy γ-radiation (^{137}Caesium source) to induce senescence "d10 senescent." Cells were harvested and subjected to downstream applications as described previously [33]. Senescence-associated β-galactosidase assay (Cell Signaling, #9860S) was performed and quantified as previously described. At least 100 cells were counted. For the EdU incorporation assay, cells were allowed to incorporate 1 μM EdU (5-ethynyl-2′-deoxyuridine, stock in DMSO) for 48 h. EdU detection was performed according to the manufacturer's protocol (Thermo Scientific, ClickiT Plus EdU Alexa Fluor 488 Imaging Kit, #C10637). At least 100 cells were quantified. To induce EGFP expression in *p16-EF/CreER*^{T2} heterozygous MEF cultures, the cells were treated with 1 μM 4-hydroxytamoxifen (OHT, Sigma #H7904) or an equivalent volume of the 100% ethanol vehicle for 48 h prior to collection and analysis.

Western blot

Immunoblot analyses were performed as described previously [80]. Immunoblots were incubated with rabbit, anti-p16 (Santa Cruz, sc-1207; 1:1000) antibody overnight and after washings, with HRP-conjugated goat, anti-rabbit antibody (Jackson Immunoresearch;1:10,000) for 3 h. Ponceau S (PonS) (0.2% w/v in 5% glacial acetic acid, Sigma-Aldrich, #P3504) served as a loading control [33].

Fibroblast isolation and culture

Dermal fibroblasts were isolated from 5-week-old C57Bl/6 female mice. Mice were euthanized, shaved, and a 1 × 2-cm section of dermal skin was removed and cut into small pieces before digestion. The dermal sections were digested for 1 h at 37 °C in 0.5 mg/mL Liberase (Roche) in serum-free RPMI (Gibco + 2 mM glutamine) shaking at ~ 150 rpm. The digestion was neutralized with complete RPMI (10% fetal bovine serum (FBS, Gibco) and 1% penicillin/streptomycin (Gibco), 1 × sodium pyruvate (100 × Gibco)), and the digested skin was pelleted via centrifugation for 5 min at 300 × *g*. The digested skin was resuspended in complete RPMI, divided into 3 T-175 flasks, and incubated at 37 °C, 5% CO_2 undisturbed for 4 days. On day 4, the cells were washed with PBS and the culture media was changed to complete MEM (10% fetal bovine serum (FBS, Gibco), 1% penicillin/streptomycin (Gibco)) to promote only fibroblast survival. Fibroblasts were then cultured in complete MEM until use.

In vitro *induction of senescence in stromal cells for co-culture*

Fibroblasts (passages 3–5), once 60–80% confluent, were placed in a minimal amount of media and an Xstrahl CIXD X-ray irradiator was used to deliver a dose of 10 Gy to the cells. The irradiated cells were washed with PBS and fresh complete MEM was

added. The irradiated cells were incubated at 37 °C 5% CO_2 for 10 days to allow for the senescent phenotype to develop. Control quiescent fibroblasts were obtained by culturing fibroblasts in low-serum MEM (0.5% fetal bovine serum (FBS, Gibco), 1% penicillin/streptomycin (Gibco)). The senescent phenotype of the irradiation-induced senescent fibroblasts was verified with β-galactosidase staining (following the manufacturers protocol (Cell BioLabs Inc.)) and compared to the control quiescent fibroblasts.

Macrophage isolation and culture

Bone marrow cells were isolated from 8-week-old C57Bl/6 female mice. Mice were euthanized and the bone marrow from both femurs was isolated. The red blood cells were lysed (BD Pharm Lyse), and the cells were passed through a 40-µm strainer. The isolated cells were washed and plated on non-tissue culture treated plates in complete RPMI (10% fetal bovine serum (FBS, Gibco), 1% penicillin/streptomycin (Gibco)) supplemented with 20 ng/mL of M-CSF (Miltenyi Biotech). On days 3 and 5, 50% of the media was removed and replenished with fresh complete RPMI supplemented with 20 ng/mL of M-CSF. On day 7, the adherent cells (differentiated macrophages) were detached using 0.25% trypsin (Gibco) and used for experiments.

Fibroblast–macrophage co-culture

Macrophages (500,000 cells/well) were plated in 12-well plates and allowed to adhere before co-culture. Fibroblasts, either quiescent control or senescent, were seeded (100,000 cells/well) onto transwell membranes (Corning) and allowed to adhere before co-culture. Upon co-culture, macrophages were either cultured alone, with quiescent fibroblasts, or with senescent fibroblasts in complete RPMI for 6 h ($n=4$ for each condition). After 6 h, the macrophages and the fibroblasts (QSN or SnC) were individually lysed and the respective RNA was isolated using the RNeasy micro kit (Qiagen) for bulk RNA sequencing.

Isolation of RNA

After collection of tissue samples, samples were submerged in TRIzol reagent, and finely minced and grinded. For in vitro cultures, media was aspirated from tissue culture plates and TRIzol added according to the manufacturer's recommended volume. The TRIzol was repeatedly pipetted across the dish. RNA isolation for both tissue and culture samples was then performed using Qiagen RNeasy Mini Kits following TRIzol extraction.

Quantitative PCR

cDNA synthesis was performed using SuperScript VILO and quantitative PCR performed using TaqMan probes and reagents with the StepOne Plus Real-Time PCR System (Thermo Fisher Scientific) with 50 ng of product per reaction. Analysis of data was performed with the delta-delta Ct method using *B2m* and *Actb* as housekeeping genes. GraphPad Prism was used to perform statistical analysis using an ANOVA followed by multiple *t*-tests with Benjamini–Hochberg multiple test correction. For RNA isolation of MEF cultures and for validation of the transgenic mouse strain, RNA extraction (Qiagen, RNeasy Mini kit, #74,104 or RNeasy Micro kit, #74,004), cDNA synthesis (Invitrogen, SuperScript III First-Strand Synthesis System, #18,080,051), and reverse transcription quantitative PCR (RT-qPCR) analysis (Applied Biosystem, SYBR Green Real-Time PCR Master Mix, #4,309,155) were performed according to manufacturer's instructions. The on-column DNase digestion step was avoided during the RNA extraction procedure. Primers were optimized via cDNA dilution series and used for RT-qPCR if efficiency achieved 90–105%. Primers were:

Bulk RNA library preparation and sequencing

After isolation of RNA as described previously, cDNA synthesis and library preparation were performed using the TruSeq RNA Library Prep Kit V2. The Agilent BioAnalyzer system was used to perform quality control on samples before and during library preparation. RNA samples with RIN scores below 7 post-cDNA synthesis were removed from analysis. Libraries were pooled and sequenced with paired-end sequencing to a depth of 50 bp for each end at a targeted depth of 30 M unique reads per sample.

Computational analysis of bulk RNA sequencing data

Reads were aligned with STAR [81] against the GENCODE [82] release M23 GRCm38.p6 genome and accompanying annotations. Differential expression

was calculated using a negative-binomial model using edgeR [83]. EnhancedVolcano [84] was used to generate volcano plots. The differential expression results were evaluated for gene set enrichment using fgsea [85] with a total of 1 billion permutations used, leading to a minimum possible p value of 1e-8 for each gene set. For the tdTom sorted bulk RNA sequencing samples, both the hallmark and gene ontology gene sets were used. For the co-culture of macrophages with senescent stromal cells, the hallmark gene sets and the predicted transcriptional targets of transcription factors of interest from Domino were used. Finally, upstream regulators of differentially expressed genes were evaluated using Ingenuity Pathways Analysis with standard settings using the differential expression test results from edgeR.

FFPE sectioning

After tissue collection, tissue was fixed in 10% NBF for 48 h. Next, tissue was rinsed in water, then rinsed twice in 1 × DPBS, each time for 15 min. Tissue was dehydrated using 70% ethanol, 80% ethanol, 95% ethanol, and 100% ethanol at room temperature, changing the solution at hourly intervals. Tissue was cleared using xylene for 1 h, followed by overnight incubation in melted paraffin wax in the oven at 55 °C. The next morning, tissue was embedded in metal molds filled with paraffin. The molds were left on the cooling plate for a few hours until paraffin solidified. The formalin-fixed paraffin-embedded blocks were removed from the mold and stored at room temperature until sectioning. Human breast capsule and mouse quadricep tissue were sectioned at 5 and 7 µm, respectively, using a microtome.

Hematoxylin and eosin staining

Slides were deparaffinized in xylene and rehydrated using decreasing concentrations of ethanol and water. Slides were incubated in Harris Hematoxylin solution (Sigma-Aldrich, product number HHS32) for 3 min and then rinsed with deionized water. Slides were washed with tap water for 5 min and immersed in 0.33% hydrogen chloride–ethanol solution until the tissue background became clear. Subsequently, slides were rinsed in Scott's tap water (Sigma-Aldrich, product number S5134) and immersed in Eosin Y solution (Sigma-Aldrich, product number HT110216) for 10 s. Lastly, slides were dehydrated in ethanol and xylene and finally mounted using Permount mounting medium (Fisher Scientific, product number SP15-100).

Masson's trichrome staining

Slides were deparaffinized in xylene and rehydrated using decreasing concentrations of ethanol and water. Slides were stained in heated Bouin's solution (Sigma-Aldrich, product number HT10132) at 56 °C for 30 min and then cooled down for 3 min inside a chemical hood. Slides were washed with tap water for 3 min to remove the yellow color from the sections. Slides were stained in Weigert's iron hematoxylin solution (Sigma-Aldrich, product number HT1079) for 5 min and washed in running tap water for 5 min. After that, slides were stained in Biebrich Scarlet-Acid Fucshin (Sigma-Aldrich, product number HT15-1) for 5 min and rinsed again in tap water until the samples had the desired color shade (light red). Subsequently, slides were stained in phosphomolybdic acid/phosphotungstic acid mix (Sigma-Aldrich, product number HT15-3 and HT15-2) for 7 min and in Aniline Blue Solution (Sigma-Aldrich, product number HT15) for 5 min. After that, slides were immersed twice in 1% acetic acid for a minute each time. Slides were rinsed in deionized water for 2 min until the water became clear and dehydrated quickly in increasing concentrations of ethanol and xylene. Slides were mounted using Permount mounting medium (Fisher Scientific, product number SP15-100).

Immunofluorescent staining

Slides were deparaffinized in xylene and rehydrated using decreasing concentrations of ethanol. Heat-induced epitope retrieval was performed in sodium citrate buffer pH 6 for mouse tissue and Tris–EDTA pH 9 for human tissue at 95 °C for 15 min. Endogenous peroxidase activity was quenched using 3% H_2O_2 in PBS for 15 min. Slides were blocked in 10% BSA and 0.05% Tween 20 in PBS for 30 min before application of one of the following antibodies: mouse anti-human $p16^{INK4a}$ (CINTEC-Roche, cat# 705–4793), rabbit anti-human alpha-smooth muscle actin or aSMA (Abcam, ab124964), mouse

anti-human CD68 (Abcam, ab955), rabbit anti-human fibroblast activation protein or FAP (Abcam, ab218164), rabbit anti-human CD31 (Abcam, ab76533), rabbit anti-mouse $p16^{INK4a}$ (Abcam, ab211542), rabbit anti-mouse CD31 (Abcam, ab182981), rabbit anti-mouse Fibromodulin or Fmod (Bioss, 12362R), and rat anti-mouse F480 (eBioscience, 14–4801-82) for 30 min at room temperature. Subsequently, slides were incubated with horseradish peroxidase (HRP) polymer-conjugated secondary antibody for 20 min and reacted with one of the tyramide signal amplification reagents including Opal 520 (Akoya, FP1487001KT), Opal 570 (Akoya, FP1488001KT), Opal 650 (Akoya, FP1496001KT) for 10 min. Subsequently, antibodies were stripped by steaming in citrate buffer at 95 °C for 15 min to allow the introduction of the next primary antibody with an Opal dye that is different from the first one. Cell nuclei were then counterstained with 4′,6-diamidino-2-phenylindole (DAPI) for 5 min before being mounted using DAKO mounting medium (Agilent, catalog no. S302380-2). Imaging of the histological samples was performed on the Microscope Axio Imager.A2 (Carl Zeiss Microscopy, LLC, model #: 490,022–0009-000) and Zeiss ZEN 3.4 (blue edition) software.

Target antigen	Target species	Host species	Host isotype	Clone	Manufacturer	Catalog #
$p16^{INK4a}$	Human	Mouse	IgG_{2a}	E6H4	CINTEC-Roche	705–4793
aSMA	Human	Rabbit	IgG	EPR5368	Abcam	124,964
CD68	Human	Mouse	IgG1	KP1	Abcam	955
FAP	Human	Rabbit	IgG	polyclonal	Abcam	218,164
CD31	Human	Rabbit	IgG	EPR3094	Abcam	76,533
$p16^{INK4a}$	Mouse	Rabbit	IgG	EPR20418	Abcam	211,542
CD31	Mouse	Rabbit	IgG	EPR17259	Abcam	182,981
Fmod	Mouse	Rabbit	IgG	polyclonal	Bioss	12362R
F480	Mouse	Rat	IgG_{2a}	BM8	eBioscience	14–4801-82

RNA fluorescence in situ *staining*

RNA fluorescence in situ (FISH) staining was performed to visualize spatial distribution of stromal and immune populations in injured murine quadricep muscles with PCL implants. RNA probe targets were selected based on differentially expressed genes identifying distinct fibroblast clusters from single-cell RNAseq analysis of sorted stromal cells from the muscle injury model. All samples were processed using ACD RNAscope HiPlex Assay protocol [86] and reagents for fixed frozen samples (ACD 324,100-UM, Cat 324,100, 324,140). In short, the injured muscles (and surrounding material implants) were harvested, fixed (10% formalin), and frozen in optimal cutting temperature (OCT) embedding media following a sucrose gradient. Tissue cryosections (14 µm, transverse orientation) were baked, post-fixed, and dehydrated prior to antigen retrieval and protease treatment. Custom HiPlex RNA probes (12 probes per assay, T1–T12) were hybridized (2 h, 40 °C) and HiPlex amplified, then probes T1–T3 were fluorophore conjugated (alternate display module: AF488, Atto550, Atto675N). Cryosections were counterstained with DAPI, mounted, and imaged with a Zeiss Axio Imager A2 (20 × objective, Zeiss ZEN 3.4 software). For subsequent rounds of probe staining (T4–T6, T7–T9, and T10–12), coverslips were removed (4 × SSC buffer), previous fluorophores cleaved (10% Cleaving Stock for 15 min, PSBT–0.5% Tween washes), new tagged-fluorophores conjugated, and cryosections imaged. RNAscope HiPlex Image Registration Software (ACD Cat. 300,065, v1) was used to register the multiple rounds of imaging based on DAPI. Image visualization was performed using Zeiss ZEN 3.4 (blue edition), Aperio ImageScope (Leica, 12.4.3.5008), and Fiji software [87]. Autofluorescence from remaining PCL particles was manually marked and masked. Overall image brightness was increased 20–40% to improve visualization of stained RNA probes.

Imaging of native tdTomato fluorescence

Muscles (and surrounding material implants) were harvested, fixed (10% paraformaldehyde), and frozen in OCT embedding media following a sucrose gradient. Tissues were sectioned at 14 µm. Cryosections were counterstained with DAPI, mounted, and imaged with a Zeiss Axio Imager A2 (20× objective, Zeiss ZEN 3.4 software).

Isolation of single-cell suspensions

All single-cell suspensions isolated from tissue samples for flow cytometry and scRNAseq were processed identically. Tissue samples were finely diced and digested in RPMI 1640 media (Gibco) with 1.6 Wunsh U/mL Liberase TL (Roche Diagnostics) and 0.2 mg/mL deoxyribonuclease I (Roche Diagnostics) for 45 min at 37 °C. Digested tissues were ground through a 100-µm then 70-µm strainer (Thermo Fisher Scientific) with excess RPMI and then washed twice with 1×PBS.

Flow cytometry and fluorescence-activated cell sorting

After isolation of single-cell suspensions, cells were washed once with DPBS and stained with LIVE/DEAD Fixable Aqua Dead Cell viability dye (Thermo Fisher Scientific) or eBioscience Fixable Viability Dye eFluor780 (Thermo Fisher Scientific) for 30 min on ice. Following incubation, the cells were washed twice with FACS buffer (1×DPBS + 1% w/v BSA (Millipore Sigma) + 1 mM EDTA) and stained for surface antigens with fluorophore-conjugated antibodies. After incubating in the dark for 45 min on ice, the cells were washed as before with FACS buffer. Samples and controls were then resuspended in FACS buffer. Data was acquired on a 4 laser Attune NxT Flow Cytometer (Thermo Fisher Scientific) and analyzed with FlowJo software (Tree Star). Compensation beads (BD Biosciences) were used at the time of data acquisition, but compensation was manually adjusted during analysis to account for the autofluorescent nature of muscle stromal cells. GraphPad Prism was used to perform statistical analysis using an ANOVA followed by multiple *t*-tests with Benjamini–Hochberg multiple test correction.

For sorting experiments, tissues were passed through 100-µm then 70-µm cell strainers (Thermo Scientific) with RPMI media then washed with FACS buffer. Cells were then stained with LIVE/DEAD Fixable Aqua Dead Cell viability dye and the appropriate fluorophore-conjugated antibodies as above. After the final wash, cells were resuspended in FACS buffer and sorted using a BD FACSAria Fusion Sorter (BD Biosciences). Cells were sorted directly into either RLT Plus Buffer (Qiagen) or 1×DPBS containing 0.01% BSA for RNA extraction or scRNAseq sequencing, respectfully.

Antibody	Manufacturer	Catalog #	Clone
Brilliant Violet 421 anti-mouse CD31	BioLegend	102,424	390
Brilliant Violet 605 anti-mouse CD45	BioLegend	103,140	30-F11
Brilliant Violet 711 anti-mouse CD11b	BioLegend	101,241	M1/70
Alexa Fluor 488 anti-mouse CD3	BioLegend	100,210	17A2
PE/Cyanine7 anti-mouse F4/80	BioLegend	123,113	BM8
APC anti-mouse CD11c	BioLegend	117,310	N418
Alexa Fluor 700 anti-mouse/rat CD29	BioLegend	102,218	HMβ1-1
Alexa Fluor 700 anti-mouse CD90.2	BioLegend	105,320	30-H12
APC-Cyanine 7 anti-mouse/rat CD29	BioLegend	102,226	HMβ1-1
TruStain FcX (anti-mouse CD16/32)	BioLegend	101,320	93

Drop-Seq single-cell RNA sequencing

Single-cell RNA sequencing data sets were collected using the Drop-Seq [42] pipeline. Cells were isolated and sorted as described in the flow cytometry methods from animals treated with decellularized extracellular matrix or PCL implants, control wounds, or naïve animals 1 or 6 weeks after surgery. Each sample was composed of three biological replicates pooled after sorting to obtain sufficient cell numbers. The single-cell suspension was manually counted and run through a microfluidic device which encapsulates the cells in aqueous droplets with barcoded beads and lysis buffer. After incubation, the emulsion is broken, beads collected, and cDNA synthesis performed with

Maxima Reverse Transcriptase. After quality control and quantification with the Agilent BioAnalyzer high-sensitivity DNA kit, whole transcriptome amplification was performed with the Kapa HiFi PCR kit. Finally, library preparation was performed with the Nextera XT kit. A detailed protocol is available from the McCarroll Lab website mccarrolllab.org/dropseq. Finally, libraries were pooled and sequenced with an Illumina NovaSeq to a target depth of 100,000 unique reads per cell.

scRNAseq computational processing

Barcode identification, alignment, and counting were performed using the McCarroll Lab's Drop-Seq toolkit following the protocol and guidelines outlined in the Drop-Seq Cookbook. Read 1 was used to identify cell and molecular barcodes by read. Read 2, containing the transcript itself, was aligned to STAR [81] using the GENCODE release M23 GRCm38.p6 genome and annotations. Unique molecular barcodes (UMI) were counted by cell barcode and cells separated from background using elbow plots of read count by barcode.

The Seurat [88] package was used for normalization, scaling, principal component analysis (PCA), clustering, and differential expression. Raw counts were first normalized to the total number of counts per cell barcode and then log scaled. Percentage of counts from mitochondrial genes and cell cycle scores were calculated with Seurat's CellCycleScoring. These parameters were then regressed from the normalized counts and the resulting residuals *z*-scored, providing scaled inputs for PCA. Thirty principal components were selected for downstream analysis using an elbow plot. The principal components were corrected for batch effect using Harmony [43] with default settings. A shared-nearest neighbor graph and Louvain clustering was then performed on the corrected principal components. Cluster number selection was performed by identifying the local maximum silhouette score within a biologically significant range of cluster numbers. Dimensional reduction for visualization was performed using the PHATE [44] python package and the uwot implementation of UMAP [89] in R. Mann–Whitney *U* test was used for differential expression in the single-cell data set. Clusters were compared to all other cells in the data set to determine characteristic genes for cluster phenotypes.

Differentiation trajectories were determined using a combination of RNA velocity, pseudotime, and CytoTRACE. Velocyto [47] was used to calculate RNA velocities as well as visualize velocities on two-dimensional cell embeddings. CytoTRACE [46] scores were calculated using default parameters. Slingshot [48] was used to calculate differentiation trajectories using initial and terminal clusters as identified by RNA velocity and CytoTRACE scores.

Comparison between data sets was performed using singleCellNet [63]. singleCellNet generates similarity scores between two data sets using all clusters present in the reference data set. For cases where discrete groups were required for analyses, each cell in the target data set was scored according to the highest score from the reference data set. For cases of comparison across species, biomaRt [90] with Ensembl annotations were used to convert murine genes to corresponding human genes or vice versa.

Intercellular signaling analysis was performed with Domino [41]. First, transcription factor activation scores are estimated using SCENIC [91]. The resulting transcription factor activation scores are correlated with receptor expression and thresholded, identifying a number of receptors correlated with activation of target transcription factors across the entire data set. Finally, candidate ligands for target receptors are pulled from the CellphoneDB2 [58] database, generating a signaling network connecting ligands with candidate receptors and their putative transcriptional targets. The transcription factors within the network are evaluated for enrichment in target clusters with Mann–Whitney *U* test to generate subnetworks targeting specific clusters.

Transfer learning for identification of SnCs from single-cell data sets

Senescent signatures were calculated using the set of differentially expressed genes from the bulk RNA sequencing comparing $p16^{+}$ and $p16^{-}$ stromal cells. The set of differentially expressed genes (FDR < 0.05) and their accompanying direction of fold change (increased or decreased in SnCs) were used. To generate a score for each cell, the *z*-scored expression values were filtered for the genes of interest, converted to indicate concordance or discordance with the direction of change in the bulk sequencing data set, and averaged. A positive resulting score indicates

a similar expression pattern to the bulk signature compared to the other cells in the single-cell data set.

Analysis of public single-cell RNA sequencing data sets

All non-VML public single-cell RNA sequencing data sets presented in this analysis provided cluster labels which were used as is with the exception of the basal cell carcinoma data set where the myofibroblast label was changed to endothelial cell based on expression of endothelial cell marker *VWF*. The data sets were also prefiltered and no further filtering was needed after visualization of total UMI count and feature count by cell. UMAP reductions were determined as described above with the exception of the removal of Harmony for batch effect correction. VML-derived scRNAseq data sets were analyzed as described above.

Statistics statement and code availability

All software used for this analysis are from publicly available packages. All statistical tests were two-tailed with each replicate representing a distinct biological sample unless otherwise specified.

Acknowledgements Biorender was used to create some of the figures presented in this manuscript. The authors thank David R. Maestas Jr. for experimental insight and advice.

Author contributions C.C., J.I.A., and J.H.E. conceptualized and drafted figures and manuscript. C.C., K.K., J.H.E, and E.J.F. formulated, performed, and interpreted computational analysis of bulk and single-cell RNA sequencing data sets. C.C., J.C.M., K.K., and J.H. performed Drop-Seq single-cell RNA sequencing. J.I.A., J.H., and L.D.H. performed the volumetric muscle loss surgeries. J.I.A., J.C.M., K.B.S., F.H., and D.M.P. performed and analyzed flow cytometry. H.H.N., A.N.P., and M.T.W. performed, imaged, and analyzed immunofluorescent staining and imaging including sectioning and sample processing. E.F.G-G. performed and analyzed in vitro co-culture experiments. A.R. performed, imaged, and analyzed fluorescence in situ hybridization staining and imaging. H.M. and J.M.v.D. designed and generated the p16-EF/CreERT2 strain, and N.H., I.S., S.T., and D.J.B. contributed to various validation experiments for this model. J.I.A. and J.H.M. performed cryosectioning and imaging of native fluorescence of the fluorescent reporter. A.J.T. and J.I.A. performed fluorescence-activated cytometric sorting. C.J.L.S. performed and analyzed Ingenuity Pathway Analysis. S.K. provided key insights to fibroblast biology that contributed to manuscript preparation and critical review. All authors participated in the construction of the manuscript and figures.

Funding This research was supported by the Department of Defense (W81XWH-17–1-0627 and W81XWH-14–1-0285), National Institutes of Health Pioneer Award DP1AR076959 (J.H.E.), Bloomberg ~ Kimmel Institute (J.H.E., D.M.P.), Morton Goldberg Professorship (J.H.E.), Bristol Myers Squib (J.H.E., D.M.P.), National Science Foundation Graduate Research Fellowship Program DGE-1746891 (A.R. and A.N.P.), NCI U01CA253403 (E.J.F.), National Institutes of Health R01 AG057493 (J.M.v.D.), and NIH T32 Training Grants 1T32AG058527-01 and 5T32CA153952-08 (J.I.A.).

Data availability The newly generated and publicly available data presented in this manuscript are available from GEO using accession numbers GSE199864 (SnC bulkRNAseq), GSE175890 (VML scRNAseq), GSE135893 (Adams et al. IPF), GSE136831 (Habermann et al. IPF), and GSE123814 (BCC scRNAseq).

Declarations

Conflict of interest J.H.E. holds equity in Unity Biotechnology and Aegeria Soft Tissue and is an advisor for Tessera Therapeutics, HapInScience, and Font Bio. D.M.P. is consultant at Aduro Biotech, Amgen, Astra Zeneca, Bayer, Compugen, DNAtrix, Dynavax Technologies Corporation, Ervaxx, FLX Bio, Immunomic, Janssen, Merck, and Rock Springs Capital. D.M.P. holds equity in Aduro Biotech, DNAtrix, Ervaxx, Five Prime therapeutics, Immunomic, Potenza, and Trieza Therapeutics. D.M.P. is a member of the scientific advisory board for Bristol Myers Squibb, Camden Nexus II, Five Prime Therapeutics, and WindMil. D.M.P. is a member of the board of directors in Dracen Pharmaceuticals. C.C. is the founder and owner of C M Cherry Consulting, LLC. E.J.F. is a member of the scientific advisory board for Resistance Bio and is a consultant for Merck and Mestag Therapeutics. J.M.v.D. is a co-founder of and holds equity in Unity Biotechnology and Cavalry Biosciences. D.J.B. is a shareholder and co-inventor on patent applications licensed to or filed by Unity Biotechnology, a company developing senolytic medicines, including small molecules that selectively eliminate senescent cells. Research in his laboratory has been reviewed by the Mayo Clinic Conflict of Interest Review Board and is being conducted in compliance with Mayo Clinic Conflict of Interest policies.

References

1. Campisi J. Aging, cellular senescence, and cancer. Annu Rev Physiol. 2013;75:685–705.
2. Childs BG, Li H, Van Deursen JM. Senescent cells: a therapeutic target for cardiovascular disease. J Clin Investig. 2018;128(4):1217–28.
3. Faust HJ, et al. IL-17 and immunologically induced senescence regulate response to injury in osteoarthritis. J Clin Investig. 2020;130(10):5493–507.
4. Howcroft TK, et al. The role of inflammation in age-related disease. Aging (Albany NY). 2013;5(1):84.

5. Jeon OH, et al. Local clearance of senescent cells attenuates the development of post-traumatic osteoarthritis and creates a pro-regenerative environment. Nat Med. 2017;23(6):775–81.
6. Jeon OH, et al. Senescence cell–associated extracellular vesicles serve as osteoarthritis disease and therapeutic markers. Jci Insight. 2019;4(7):e125019.
7. Minamino T, et al. A crucial role for adipose tissue p53 in the regulation of insulin resistance. Nat Med. 2009;15(9):1082–7.
8. Muñoz-Espín D, et al. Programmed cell senescence during mammalian embryonic development. Cell. 2013;155(5):1104–18.
9. Storer M, et al. Senescence is a developmental mechanism that contributes to embryonic growth and patterning. Cell. 2013;155(5):1119–30.
10. Coppé J-P, et al. Senescence-associated secretory phenotypes reveal cell-nonautonomous functions of oncogenic RAS and the p53 tumor suppressor. PLoS Biol. 2008;6(12):e301.
11. Tchkonia T, et al. Cellular senescence and the senescent secretory phenotype: therapeutic opportunities. J Clin Investig. 2013;123(3):966–72.
12. Wan M, Gray-Gaillard EF, Elisseeff JH. Cellular senescence in musculoskeletal homeostasis, diseases, and regeneration. Bone Res. 2021;9(1):1–12.
13. Bai H, et al. Suppression of transforming growth factor-β signaling delays cellular senescence and preserves the function of endothelial cells derived from human pluripotent stem cells. Stem Cells Transl Med. 2017;6(2):589–600.
14. Dumont P, et al. Induction of replicative senescence biomarkers by sublethal oxidative stresses in normal human fibroblast. Free Radical Biol Med. 2000;28(3):361–73.
15. Hooten NN, Evans MK. Techniques to induce and quantify cellular senescence. JoVE (Journal of Visualized Experiments). 2017;123:e55533.
16. Amor C, et al. Senolytic CAR T cells reverse senescence-associated pathologies. Nature. 2020;583(7814):127–32.
17. Kim KM, et al. Identification of senescent cell surface targetable protein DPP4. Genes Dev. 2017;31(15):1529–34.
18. Poblocka M, et al. Targeted clearance of senescent cells using an antibody-drug conjugate against a specific membrane marker. Sci Rep. 2021;11(1):1–10.
19. Buechler MB, et al. Cross-tissue organization of the fibroblast lineage. Nature. 2021;593(7860):575–9.
20. Wei K, et al. Notch signalling drives synovial fibroblast identity and arthritis pathology. Nature. 2020;582(7811):259–64.
21. Elyada E, et al. Cross-species single-cell analysis of pancreatic ductal adenocarcinoma reveals antigen-presenting cancer-associated fibroblasts. Cancer Discov. 2019;9(8):1102–23.
22. Chung L, et al. Interleukin 17 and senescent cells regulate the foreign body response to synthetic material implants in mice and humans. Sci Transl Med. 2020;12(539):eaax3799.
23. Demaria M, et al. An essential role for senescent cells in optimal wound healing through secretion of PDGF-AA. Dev Cell. 2014;31(6):722–33.
24. Hwang B, Lee JH, Bang D. Single-cell RNA sequencing technologies and bioinformatics pipelines. Exp Mol Med. 2018;50(8):1–14.
25. Stein-O'Brien GL, et al. Decomposing cell identity for transfer learning across cellular measurements, platforms, tissues, and species. Cell Syst. 2019;8(5):395-411.e8.
26. Taroni JN, et al. MultiPLIER: a transfer learning framework for transcriptomics reveals systemic features of rare disease. Cell Syst. 2019;8(5):380-394.e4.
27. Selman M, Pardo A. Fibroageing: an ageing pathological feature driven by dysregulated extracellular matrix-cell mechanobiology. Ageing Res Rev. 2021;70:101393.
28. Omori S, et al. Generation of a p16 reporter mouse and its use to characterize and target p16(high) cells in vivo. Cell Metab. 2020;32(5):814-828 e6.
29. Liu JY, et al. Cells exhibiting strong p16(INK4a) promoter activation in vivo display features of senescence. Proc Natl Acad Sci U S A. 2019;116(7):2603-2611.
30. Scarff KL, et al. A retained selection cassette increases reporter gene expression without affecting tissue distribution in SPI3 knockout/GFP knock-in mice. Genesis: J Gen Dev. 2003;36(3):149–57.
31. Schmidt-Supprian M, Wunderlich FT, Rajewsky K. Excision of the Frt-flanked neo (R) cassette from the CD19cre knock-in transgene reduces Cre-mediated recombination. Transgenic Res. 2007;16(5):657–60.
32. Baker DJ, et al. Naturally occurring p16(Ink4a)-positive cells shorten healthy lifespan. Nature. 2016;530(7589):184–9.
33. Sturmlechner I, et al. p21 produces a bioactive secretome that places stressed cells under immunosurveillance. Science. 2021;374(6567):eabb3420.
34. Childs BG, et al. Senescent intimal foam cells are deleterious at all stages of atherosclerosis. Science. 2016;354(6311):472–7.
35. Wiley CD, et al. SILAC analysis reveals increased secretion of hemostasis-related factors by senescent cells. Cell Rep. 2019;28(13):3329-3337.e5.
36 Frangogiannis NG. Transforming growth factor-β in tissue fibrosis. J Exp Med. 2020;217(3):e20190103.
37. Rice LM, et al. Fresolimumab treatment decreases biomarkers and improves clinical symptoms in systemic sclerosis patients. J Clin Investig. 2015;125(7):2795–807.
38. Sanderson N, et al. Hepatic expression of mature transforming growth factor beta 1 in transgenic mice results in multiple tissue lesions. Proc Natl Acad Sci 1995;92(7):2572-2576.
39. Sime PJ, et al. Adenovector-mediated gene transfer of active transforming growth factor-beta1 induces prolonged severe fibrosis in rat lung. J Clin Investig. 1997;100(4):768–76.
40. Sonnylal S, et al. Postnatal induction of transforming growth factor β signaling in fibroblasts of mice recapitulates clinical, histologic, and biochemical features of scleroderma. Arthritis Rheum. 2007;56(1):334–44.
41. Cherry C, et al. Computational reconstruction of the signalling networks surrounding implanted biomaterials from single-cell transcriptomics. Nat Biomed Eng. 2021;5(10):1228–38.
42. Macosko EZ, et al. Highly parallel genome-wide expression profiling of individual cells using nanoliter droplets. Cell. 2015;161(5):1202–14.
43. Korsunsky I, et al. Fast, sensitive and accurate integration of single-cell data with Harmony. Nat Methods. 2019;16(12):1289–96.

44. Moon KR, et al. Visualizing structure and transitions in high-dimensional biological data. Nat Biotechnol. 2019;37(12):1482–92.
45. Becht E, et al. Dimensionality reduction for visualizing single-cell data using UMAP. Nat Biotechnol. 2019;37(1):38–44.
46. Gulati GS, et al. Single-cell transcriptional diversity is a hallmark of developmental potential. Science. 2020;367(6476):405–11.
47. La Manno G, et al. RNA velocity of single cells. Nature. 2018;560:494 (Nature Publishing Group).
48. Street K, et al. Slingshot: cell lineage and pseudotime inference for single-cell transcriptomics. BMC Genomics. 2018;19(1):1–16.
49. Cheng F, et al. Vimentin coordinates fibroblast proliferation and keratinocyte differentiation in wound healing via TGF-β–Slug signaling. Proc Natl Acad Sci 2016;113(30):E4320-E4327.
50. Kahounová Z, et al. The fibroblast surface markers FAP, anti-fibroblast, and FSP are expressed by cells of epithelial origin and may be altered during epithelial-to-mesenchymal transition. Cytometry Part A. 2018;93(9):941–51.
51. Muhl L, et al. Single-cell analysis uncovers fibroblast heterogeneity and criteria for fibroblast and mural cell identification and discrimination. Nat Commun. 2020;11(1):1–18.
52. Schmidt M, et al. Controlling the balance of fibroblast proliferation and differentiation: impact of Thy-1. J Investig Dermatol. 2015;135(7):1893–902.
53. Brandt MM, et al. Transcriptome analysis reveals microvascular endothelial cell-dependent pericyte differentiation. Sci Rep. 2019;9(1):1–12.
54. Kumar A, et al. Specification and diversification of pericytes and smooth muscle cells from mesenchymoangioblasts. Cell Rep. 2017;19(9):1902–16.
55. Mitchell TS, et al. RGS5 expression is a quantitative measure of pericyte coverage of blood vessels. Angiogenesis. 2008;11(2):141–51.
56 Hernandez-Segura A, et al. Unmasking transcriptional heterogeneity in senescent cells. Curr Biol. 2017;27(17):2652-2660.e4.
57. Jun J-I, Lau LF. CCN2 induces cellular senescence in fibroblasts. J Cell Commun Signal. 2017;11(1):15–23.
58. Efremova M, et al. Cell PhoneDB: inferring cell–cell communication from combined expression of multi-subunit ligand–receptor complexes. Nat Protoc. 2020;15(4):1484–506.
59. Howe KL, et al. Ensembl 2021. Nucleic Acids Res. 2021;49(D1):D884–91.
60. Adams TS, et al. Single-cell RNA-seq reveals ectopic and aberrant lung-resident cell populations in idiopathic pulmonary fibrosis. Sci Adv. 2020;6(28):eaba1983.
61. Habermann AC, et al. Single-cell RNA sequencing reveals profibrotic roles of distinct epithelial and mesenchymal lineages in pulmonary fibrosis. Sci Adv. 2020;6(28):eaba1972.
62. Yost KE, et al. Clonal replacement of tumor-specific T cells following PD-1 blockade. Nat Med. 2019;25(8):1251–9.
63 Tan Y, Cahan P. SingleCellNet: a computational tool to classify single cell RNA-Seq data across platforms and across species. Cell Syst. 2019;9(2):207-213.e2.
64. Jetten AM. GLIS1–3 transcription factors: critical roles in the regulation of multiple physiological processes and diseases. Cell Mol Life Sci. 2018;75(19):3473–94.
65. Liu S, et al. miR-106b-5p targeting SIX1 inhibits TGF-β1-induced pulmonary fibrosis and epithelial-mesenchymal transition in asthma through regulation of E2F1. Int J Mol Med. 2021;47(3):1–1.
66. Vuga LJ, et al. Cartilage oligomeric matrix protein in idiopathic pulmonary fibrosis. PLoS ONE. 2013;8(12):e83120.
67. Jun J-I, Lau LF. Taking aim at the extracellular matrix: CCN proteins as emerging therapeutic targets. Nat Rev Drug Discov. 2011;10(12):945–63.
68. Valentijn FA, et al. CCN2 aggravates the immediate oxidative stress–DNA damage response following renal ischemia–reperfusion injury. Antioxidants. 2021;10(12):2020.
69. Dwivedi N, et al. Epithelial vasopressin type-2 receptors regulate myofibroblasts by a YAP-CCN2–dependent mechanism in polycystic kidney disease. J Am Soc Nephrol. 2020;31(8):1697–710.
70. Mascharak S, et al. Multi-omic analysis reveals divergent molecular events in scarring and regenerative wound healing. Cell Stem Cell. 2022;29:315.
71 Zhou X, et al. Microenvironmental sensing by fibroblasts controls macrophage population size. bioRxiv. 2022;15:e1006577.
72. Diekman BO, et al. Expression of p16 INK 4a is a biomarker of chondrocyte aging but does not cause osteoarthritis. Aging Cell. 2018;17(4):e12771.
73. Dondossola E, et al. Examination of the foreign body response to biomaterials by nonlinear intravital microscopy. Nat Biomed Eng. 2016;1(1):1–10.
74. Stockmann C, et al. A wound size-dependent effect of myeloid cell-derived vascular endothelial growth factor on wound healing. J Investig Dermatol. 2011;131(3):797–801.
75. Willenborg S, et al. CCR2 recruits an inflammatory macrophage subpopulation critical for angiogenesis in tissue repair. Blood, J Am Soc Hematol. 2012;120(3):613–25.
76. Casella G, et al. Transcriptome signature of cellular senescence. Nucleic Acids Res. 2019;47(21):11476.
77. Saul D, et al. A new gene set identifies senescent cells and predicts senescence-associated pathways across tissues. Nat Commun. 2022;13(1):4827.
78. Kim JH, et al. High cleavage efficiency of a 2A peptide derived from porcine teschovirus-1 in human cell lines, zebrafish and mice. PLoS ONE. 2011;6(4):e18556.
79. Baker DJ, et al. Opposing roles for p16 Ink4a and p19 Arf in senescence and ageing caused by BubR1 insufficiency. Nat Cell Biol. 2008;10(7):825–36.
80. Kasper LH, et al. CREB binding protein interacts with nucleoporin-specific FG repeats that activate transcription and mediate NUP98-HOXA9 oncogenicity. Mol Cell Biol. 1999;19(1):764–76.
81. Dobin A, et al. STAR: ultrafast universal RNA-seq aligner. Bioinformatics. 2013;29(1):15–21.
82. Frankish A, et al. GENCODE 2021. Nucleic Acids Res. 2021;49(D1):D916–23.
83. Robinson MD, McCarthy DJ, Smyth GK. edgeR: a Bioconductor package for differential expression analysis of digital gene expression data. Bioinformatics. 2010;26(1):139–40.

84. Blighe K, Rana S, and Lewis M. EnhancedVolcano: publication-ready volcano plots with enhanced colouring and labeling. R package version 1.6. 0. 2020 https://github.com/kevinblighe/EnhancedVolcano.
85. Korotkevich G, et al. Fast gene set enrichment analysis. bioRxiv. 2021;060012.
86. Wang F, et al. RNAscope: a novel in situ RNA analysis platform for formalin-fixed, paraffin-embedded tissues. J Mol Diagn. 2012;14(1):22–9.
87. Schindelin J, et al. Fiji: an open-source platform for biological-image analysis. Nat Methods. 2012;9(7):676–82.
88. Hao Y, et al. Integrated analysis of multimodal single-cell data. Cell. 2021;184(13):3573-87
89. McInnes L, Healy J, and Melville J. Umap: Uniform manifold approximation and projection for dimension reduction. arXiv preprint arXiv:1802.03426, 2018.
90. Smedley D, et al. BioMart–biological queries made easy. BMC Genomics. 2009;10(1):1–12.
91. Aibar S, et al. SCENIC: single-cell regulatory network inference and clustering. Nat Meth. 2017;14(11):1083–6.